

# Properties of Galactic early-type O-supergiants

## A combined FUV-UV and optical analysis <sup>★</sup>

J.-C. Bouret<sup>1</sup>, D. J. Hillier<sup>2</sup>, T. Lanz<sup>3</sup>, A. W. Fullerton<sup>4</sup>

<sup>1</sup> Laboratoire d'Astrophysique de Marseille, Université d'Aix-Marseille & CNRS, UMR7326, 38 rue F. Joliot-Curie, F-13388 Marseille Cedex 13, France, e-mail: Jean-Claude.Bouret@oamp.fr

<sup>2</sup> Department of Physics and Astronomy, University of Pittsburgh, Pittsburgh, PA 15260, USA

<sup>3</sup> Laboratoire J.-L. Lagrange, UMR 7293, Université de Nice-Sophia Antipolis, CNRS, Observatoire de la Côte d'Azur, B.P. 4229, F-06304 Nice Cedex 4, France

<sup>4</sup> Space Telescope Science Institute, 3700 San Martin Drive, Baltimore, MD 21218, USA

Accepted May 3rd 2012

### ABSTRACT

**Aims.** We aim to constrain the properties and evolutionary status of early and mid-spectral type supergiants (from O4 to O7.5). These possess the highest mass-loss rates among the O stars, and exhibit conspicuous wind profiles.

**Methods.** Using the non-LTE wind code CMFGEN we simultaneously analyzed the FUV-UV and optical spectral range to determine the photospheric properties and wind parameters. We derived effective temperatures, luminosities, surface gravities, surface abundances, mass-loss rates, wind terminal velocities, and clumping filling factors.

**Results.** The supergiants define a very clear evolutionary sequence, in terms of ages and masses, from younger and more massive stars to older stars with lower initial masses. O4 supergiants cluster around the 3 Myr isochrone and are more massive than  $60 M_{\odot}$ , while the O5 to O7.5 stars have masses in the range 50 -  $40 M_{\odot}$  and are  $4 \pm 0.3$  Myr old. The surface chemical composition is typical of evolved O supergiants (nitrogen-rich, carbon- and oxygen-poor). While the observed ranges of carbon and nitrogen mass-fractions are compatible with those expected from evolutionary models for the measured stellar masses, the N/C ratios as a function of age are inconsistent with the theoretical predictions for the four earliest (O4 spectral type) stars of the sample. We question the efficiency of rotational mixing as a function of age for these stars and suggest that another mechanism may be needed to explain the observed abundance patterns. Mass-loss rates derived with clumped-models range within a factor of three of the theoretical mass-loss rates. The corresponding volume-filling factors associated with small-scale clumping are  $0.05 \pm 0.02$ . Clumping is found to start close to the photosphere for all but three stars, two of which are fast rotators.

**Key words.** Stars: winds – Stars: atmospheres – Stars: early-type – Stars: fundamental parameters

## 1. Introduction

Many fields of modern astrophysics are directly or indirectly related to the physics of massive stars. Locally, massive stars are responsible for the ionization and expansion of their surrounding HII regions, and are believed to be responsible for triggering star formation (e.g. Zavagno et al. 2007; Martins et al. 2010). More generally, they dominate the chemical and dynamical evolution of the global interstellar medium of their host galaxies. Starburst events, either in the local or the distant universe, are dominated by hot massive stars, as revealed by the composite spectrum of distant, star-forming galaxies, which exhibit numerous features typical of O and B stars (e.g. Steidel et al. 1996). Fast rotating massive stars are likely progenitors of some of the most energetic events in the Universe, such as core-collapse supernovae and gamma-ray-bursts (GRBs) (e.g. Hjorth et al. 2003;

Woosley & Bloom 2006) and population III stars are believed to be very massive objects with extreme effective temperatures (Bromm et al. 1999; Nakamura & Umemura 1999).

In the 1970s it was recognized that stellar evolution in the upper Hertzsprung-Russell (H-R) diagram is, to a large extent, governed by mass loss. Through the course of their evolution, massive stars lose a significant fraction of their mass through their stellar winds (see e.g., the review by Meynet & Maeder 2007), and through giant eruptions (e.g. Smith & Owocki 2006). Although the line-driven wind theory has been successful in explaining the global behavior of stellar winds, the actual wind parameters remain subject to uncertainties, especially regarding the wind terminal velocity, mass-loss rate and the degree of clumpiness (see e.g., the workshop held in 2007 in Potsdam, Hamann et al. 2008). The most striking uncertainty regarding the mass-loss rates is related to the intrinsically unstable nature of the line-driving mechanism (Lucy & Solomon 1970; Owocki et al. 1988), which leads to strong reverse shocks (e.g. Owocki & Puls 1999) that separate fast low-density wind material from overdense clumps. Since many prominent mass-loss diagnostics are sensitive to the square of the density, they overestimate the mass-loss rate in the presence of clumping. The uncertainty in the true value of the mass-loss rate translates in a corresponding uncertainty in the evolutionary tracks of massive stars.

Send offprint requests to: J.-C. Bouret

<sup>★</sup> Based on observations made with the NASA-CNES-CSA *Far Ultraviolet Spectroscopic Explorer (FUSE)* and by the NASA-ESA-SERC *International Ultraviolet Explorer (IUE)*, and retrieved from the Multimission Archive at the Space Telescope Science Institute (MAST). Based on observations collected with the ELODIE spectrograph on the 1.93-m telescope (Observatoire de Haute-Provence, France). Based on observations collected with the FEROS instrument on the ESO 2.2 m telescope, program 074.D-0300 and 075.D-0061.

Recent studies showed that winds are clumped, although there is no consensus concerning the amount, nature (optically thin versus optically thick) and stratification of clumping. Initial studies (Crowther et al. 2002; Hillier et al. 2003; Bouret et al. 2003, 2005; Fullerton et al. 2006) found a reduction in mass-loss rates by a factor of three to ten when using the optically thin assumption for clumping. Within the same framework, the radial distribution of the clumping factor was constrained by Puls et al. (2006) and Najarro et al. (2011), based on a simultaneous modeling of H $\alpha$  infrared, millimeter and radio observations. These studies concluded that clumping is three to six times stronger in the lower wind, where H $\alpha$  forms, compared with the outer wind, where the radio continuum originates. These findings marginally agree with the theoretical predictions by Runacres & Owocki (2002, 2005). The aforementioned studies assumed a void-interclump medium, although Zsargó et al. (2008) demonstrated that the treatment of a non-void interclump medium is required to explain the global spectroscopic properties of massive stars.

The optically thin approximation was subsequently challenged by Oskinova et al. (2007), who claimed that significantly lower reduction (factor of three only) is found when using optically thick clumping. When it is pronounced, this macroclumping (or porosity) affects the emerging spectrum for a given mass-loss by reducing the effective opacity of the wind, because optically thick clumps hide material. Another factor that might affect the mass-loss rate is the structure of winds in velocity space (hereafter called velocity porosity). This arises because the dense absorbing clumps along a given line of sight, only occur at discrete velocities, and leads to a reduction in the strength of P Cygni absorption components (Owocki 2008). This velocity porosity has been implemented in 2D/3D stochastic wind models by Sundqvist et al. (2010, 2011), who concluded that it could increase mass-loss rates derived from UV resonance lines by up to an order of magnitude.

Major progress has also been achieved in the last few years in stellar rotation theory, but more progress is needed. It has been known for a long time that the physical properties of stars are distorted by rotation, as predicted from the von Zeipel theorem and indicated from recent interferometric studies (e.g. Domiciano de Souza et al. 2003). Consequently, rotation is also expected to cause a latitudinal dependence of the line force and hence mass loss (Maeder & Meynet 2000).

From the view point of stellar evolution, rotation causes an increase in the mass-loss rate, a change in evolutionary tracks in the H-R diagram, a lowering of the effective gravity, an extension of the main-sequence phase, the transport of angular momentum and the mixing of CNO-cycle processed material up to the stellar surface (Maeder & Meynet 2000; Heger & Langer 2000). The so-called helium discrepancy first identified by Herrero et al. (1992) in many galactic O-type stars and especially in fast rotators is naturally explained by evolution models with rotation — higher helium (and nitrogen) abundances are predicted for higher masses and higher rotation velocities. Another consequence of rotation is that two stars at the same evolutionary phase and at the same location in the H-R diagram can have different initial masses.

Several other observational facts have been successfully accounted for using evolutionary models with rotation (Maeder & Meynet 2000). Models with rotation predict the correct blue-to-red supergiant ratio as observed in the Small Magellanic Cloud (Maeder & Meynet 2001), explain the observed population of Wolf-Rayet stars as a function of metallicity (Meynet & Maeder 2003, 2005), and provide a consistent framework for the evo-

lution of progenitors of soft-long GRBs (Yoon & Langer 2005; Woosley & Bloom 2006; Meynet & Maeder 2007).

Despite these success, some observations remain unexplained. Hunter et al. (2007, 2008, 2009), who investigated the link between surface abundance patterns and rotation in the Galaxy and in the Magellanic Clouds, concluded that up to 40% of their sample presented nitrogen surface abundances that could not be explained by rotational mixing. These studies strongly suggest that the global chemical evolution of massive stars, as probed from their surface abundances, is an intricate combination of several physical parameters, including mass, metallicity, age (evolutionary status) and rotation (Maeder et al. 2009).

Some of the spectral lines used to determine mass-loss rates and clumping factors originate from CNO ions. Because surface CNO abundance patterns are modified by rotational mixing during stellar evolution, it is very important to have reliable estimates of these patterns in order to fully characterize the wind properties of O-type stars.

For this study, we have analyzed a sample consisting of eight Galactic supergiants with spectral types ranging from O4 If to O7.5 If (Sota et al. 2011). We derive their properties, and address questions about as their evolutionary status and how their surface abundances relate to this. We also investigate whether a consistent picture for mass loss and clumping may be drawn from different diagnostics such as P v  $\lambda\lambda 1118-1128$ , O v  $\lambda 1371$ , N iv  $\lambda 1718$ , He ii  $\lambda 4686$  and H $\alpha$ . By using different diagnostics we can test the influence of the ionization structure, the adopted abundances, and to a limited extent, the clumping formulation on wind diagnostics.

In the following section, we present our sample selection and observational material. The modeling tools are presented in Sect. 3, while diagnostics of the different stellar parameters are presented in Sect. 4. Results of the analysis for the individual objects are presented in Sect. 5 and a general discussion of the evolutionary status, chemical properties and wind properties is given in Sect. 6, before our general conclusion in Sect 7.

## 2. Target selection and observations

### 2.1. Stellar sample

Table 1 presents the sample selected for this study and fundamental observational data. The selected objects are considered to be representative of early-Of supergiants, whose surface properties are likely to show processed material from stellar evolution and whose strong winds are expected to exhibit conspicuous signatures of clumping. The spectral classification scheme of these stars was designed by Walborn (1971a,b, 1973) and was recently updated in Sota et al. (2011). The scheme is meant to sort stars with different temperatures, luminosities, and abundances. CNO-cycled material must play a role in explaining the observed dispersion for a given spectral type/luminosity class.

We checked that binarity is not a problem for our spectroscopic analyses. De Becker et al. (2009) concluded that HD 15570, HD 16691, and HD 14947 are very likely single because the authors did not find signs of radial velocity variations that they could unambiguously relate to companions. HD 66811 has been extensively observed but no companions have been detected for this star, even in high-sensitivity speckle surveys for binarity (see e.g. Mason et al. 1998). The adaptive optics survey for faint companions led by Turner et al. (2008) also concluded that HD 210839, HD 192639 and HD 163758 are single stars. HD 190429 is a well-known binary but the spectrum (and the photometry) we used was for HD 190429A (i.e., for the primary

**Table 1.** Basic parameters of our targets.

Star	Other name	Spectral Type	<i>U</i>	<i>B</i>	<i>V</i>	<i>J</i>	<i>H</i>	<i>K</i>	<i>E(B - V)</i>	dist. (kpc)	<i>M<sub>V</sub></i>
HD 16691	...	O4 If	8.620	9.182	8.702	7.653	7.444	7.362	0.800	3.31±0.20	-6.38 <sup>+0.12</sup> <sub>-0.14</sub>
HD 66811	ζ Pup	O4 I(n)fp	0.890	1.941	2.210	2.790	2.955	2.968	0.040	0.46±0.04	-6.23 <sup>+0.17</sup> <sub>-0.20</sub>
HD 190429A	...	O4 If	....	7.201	7.088	6.189	6.162	6.150	0.460	2.45±0.20	-6.28 <sup>+0.21</sup> <sub>-0.24</sub>
HD 15570	...	O4 If	8.391	8.796	8.110	6.477	6.310	6.158	0.966	2.34±0.11	-6.73 <sup>+0.11</sup> <sub>-0.14</sub>
HD 14947	...	O4.5 If	7.850	8.452	7.998	7.037	6.945	6.861	0.730	3.00±0.20	-6.43 <sup>+0.14</sup> <sub>-0.15</sub>
HD 210839	λ Cep	O6 I(n)fp	4.620	5.242	5.050	5.053	4.618	4.500	0.513	0.95±0.10	-6.43 <sup>+0.11</sup> <sub>-0.12</sub>
HD 163758	...	O6.5 If	6.458	7.346	7.318	7.194	7.163	7.157	0.300	3.60±0.20	-6.39 <sup>+0.12</sup> <sub>-0.17</sub>
HD 192639	...	O7.5 Iabf	6.830	7.455	7.116	6.300	6.271	6.217	0.620	2.00±0.20	-6.31 <sup>+0.17</sup> <sub>-0.23</sub>

Note : Spectral types are taken from Sota et al. (2011), while the photometry is taken from the GOS catalog (Maíz-Apellániz et al. 2004). Reddening, absolute magnitude and distances are calculated using the procedure presented in Sect. 4.1.

only). Because the companion, HD 190429B, has a spectral type of O9.5II, the luminosity difference is about 0.7 dex (Walborn & Howarth 2000), implying that its contribution to the total flux remains small.

The log of the spectroscopic observations is presented in Table 2.

## 2.2. FUV and UV data

We extracted short wavelength, high-resolution echelle (SWP) *IUE* spectra from MAST. The SWP spectra cover the spectral range,  $\lambda\lambda 1150\text{--}2000\text{ \AA}$ , at a resolving power  $R = 10,000$ . Only one SWP spectrum is available for HD 14947, HD 15570, HD 16691, HD 163758 and HD 192639, respectively. For HD 190429A, we used the co-added spectrum presented in Bouret et al. (2005). For λ Cep we selected the only *IUE* SWP high-resolution spectrum that is not saturated (see Bianchi & Garcia 2002).

As part of the *IUE* “MEGA” campaign (Massa et al. 1995; Howarth et al. 1995), ζ Puppis was observed over nineteen days, corresponding to slightly more than three rotation periods (5.2 days). We chose to stick to the MEGA campaign to avoid any problems with “long-term” variations, which have not been studied extensively. For the 107 spectra from this campaign, we constructed three mean spectra - one for each “rotational” cycle. Because these three spectra were very similar, we averaged all of them to form the spectrum that is used in our analysis.

We furthermore smoothed the spectra to a resolution of  $40\text{ km s}^{-1}$  to increase the signal-to-noise ratio. The spectra of all stars show many narrow lines of interstellar origin. This interstellar contamination dominates the whole UV spectrum of HD 15570; only strong lines such as C IV  $\lambda\lambda 1548\text{--}1550$  or N IV  $\lambda 1718$  can be used safely for this star.

All stars but HD 66811 were observed with *FUSE* through the LWRS  $30'' \times 30''$  aperture. The nominal spectral resolution is 20,000, or about  $20\text{ km s}^{-1}$ , and the wavelength range extends from  $905\text{ \AA}$  to  $1187\text{ \AA}$ . The processed *FUSE* spectra were retrieved from MAST and reprocessed with the final version of the *FUSE* pipeline CalFUSE 3.2.3. Individual sub-exposures were co-added for each segment and then merged to form a single spectrum, using Lindler’s FUSE-REGISTER program. We avoided contamination by the “worm” artifact (Sahnou et al. 2000) by using only the LiF2A spectra on the long-wavelength side ( $\lambda\lambda 1086\text{--}1183\text{ \AA}$ ) of the spectrum. Finally, the co-added merged spectra were smoothed to a resolution of  $30\text{ km s}^{-1}$  to enhance the signal-to-noise ratio.

For HD 66811, we used the *Copernicus* spectra already dis-

cussed in Pauldrach et al. (1994) that were originally obtained by Morton & Underhill (1977), to which we refer the reader for details concerning the observations and data reduction.

## 2.3. Optical data

For all but one of the northern stars, we used data obtained in November 2004 with the *ELODIE* spectrograph, which was mounted on the 193cm telescope at Observatoire de Haute-Provence (*OHP*). The resolving power is 42,000 and the wavelength coverage extends from  $3895\text{ \AA}$  to  $6815\text{ \AA}$ . The exposure times were chosen to ensure a signal-to-noise ratio of at least 100 at  $5200\text{ \AA}$ . The reduction of spectroscopic data acquired with *ELODIE* was performed using the standard reduction pipeline described in Baranne et al. (1996). Each order was normalized by a fit to the continuum, which was specified by fitting a smooth spline to carefully selected continuum windows. This step was then followed by a complete merging of successive orders to reconstruct the full spectrum for each star.

The spectrum of λ Cep was collected with the NARVAL spectropolarimeter at Telescope Bernard Lyot (TBL) at Pic du Midi Observatory in December 2006. The resolving power is  $R=65,000$  for a wavelength coverage  $3700\text{--}10050\text{ \AA}$ . The set of four sub-exposures was processed using Libre ESPrIT (Donati et al. 1997), a fully automatic reduction package installed at TBL for optimal extraction of NARVAL spectra. The signal-to-noise ratios per  $2.6\text{ km s}^{-1}$  velocity bin range from 400 to 1100 over the  $3800\text{--}7000\text{ \AA}$  range that we used here.

The spectrum of HD 163758 was extracted from the UVES Paranal Observatory Project, a program of acquisition, reduction, and public release of stellar spectra obtained with UVES at the VLT (Bagnulo et al. 2003). Complete details concerning these data can be found at the *UVES POP* URL<sup>1</sup>. The spectrum was normalized by fitting a spline to the continuum, which was defined by the same windows used to normalize the *ELODIE* spectra.

The other southern star of this sample, namely ζ Puppis, was observed with the *FEROS* spectrograph on the MPI 2.2m telescope at La Silla Observatory (prog. ID 074.D-0300(A)). The spectrum coverage is from  $3800$  to  $8800\text{ \AA}$ , with a resolving power of 48,000. The spectrum was wavelength-calibrated and extracted using a modified *FEROS* pipeline that includes the modifications already described in Sana et al. (2006) and Sana (2009).

<sup>1</sup> <http://www.sc.eso.org/santiago/uvespop/>

**Table 2.** Star sample and observations logs.

Star	Spectral Type	FUV		UV		Optical	
		Data Set <sup>a</sup>	Date	Data Set	Date	Instrument	Date
HD 16691	O4 If	F - E8050101	2004-11-18	SWP46545	1992-12-21	OHP/ELODIE	2005-11-05
HD 66811	O4 I(n)fp	C - C044-001	1973-02-22	SWP15296	1981-10-20	ESO/FEROS	2005-12-20
HD 190429A	O4 If	F - P1028401	2000-07-18	SWP <sup>b</sup> .....	...	OHP/ELODIE	2004-08-27
HD 15570	O4 If	F - E0820101	2005-11-08	SWP11234	1981-02-04	OHP/ELODIE	2004-11-17
HD 14947	O4.5 If	F - E0820201	2004-30-09	SWP10724	1980-12-01	OHP/ELODIE	2004-11-20
HD 210839	O6 I(n)fp	F - P1163101	2000-07-22	SWP52623	1994-10-23	TBL/NARVAL	2006-12-13
HD 163758	O6.5 If	F - P1015901	2000-08-16	SWP02892	1978-10-09	ESO/UVES	2001-07-27
objectobjectHD 192639	O7.5 Iabf	F-C17101010	2002-09-04	SWP09493	1980-07-11	OHP/ELODIE	2001-08-11

<sup>a</sup> Observatory used to obtain spectra: F *FUSE*; C *Copernicus*

<sup>b</sup> Co-addition of several spectra; see Bouret et al. (2005)

Some broad spectral lines like the He II  $\lambda 4686$  line in the *FEROS* spectrum of  $\zeta$  Puppis or the H $\alpha$  line in either *ELODIE* or *FEROS* spectra extend over two adjacent orders. In these cases, we found that adopting order shapes from adjacent orders gave the best continuum reduction.

#### 2.4. Some considerations about spectroscopic variability

The observations used for this study have been obtained at very different epochs for each star (see Table 2). Therefore, we had to address the problem of the expected variability of the stellar winds, and particular how this would affect the physical quantities that we measured through spectral fitting.

Resonance line variations are well documented for several O-type stars in the FUV-UV range, including two of our targets, namely  $\zeta$  Puppis and  $\lambda$  Cep. For the other stars only one FUV-UV spectrum has been obtained, and hence no information is available on the UV variability of their wind or photosphere. The most prominent signature of variable wind structures in hot stars is the presence of blueward-migrating “discrete absorption components” (DACs), which are clearly visible in time-series IUE spectra (e.g. Howarth et al. 1995; Massa et al. 1995). These data have established that the variations in the wind lines are not chaotic fluctuations, but are instead very systematic and probably associated with large-scale perturbations that arise from corotating interacting regions (Cranmer & Owocki 1996).

In the optical range short-timescale (of about hours) stochastic spectral line variations of H $\alpha$  and He II  $\lambda 4686$  are well documented for O-type stars (e.g. Prinja & Fullerton 1994; Eversberg et al. 1998; Markova et al. 2005; De Becker et al. 2009). This variability is commonly attributed to the small-scale structures, or clumps, which are predicted by time-dependent models of the line-driven instability (Owocki 1994; Dessart & Owocki 2003, 2005), though pulsations might also be involved at some level (e.g. Markova 2002; Prinja et al. 2006). The observed line profile variability indicates that the winds are not smooth, but perturbed. Observations furthermore showed that significant variations in H $\alpha$  start from the wind base up to velocities of a few hundreds of km s<sup>-1</sup>, which corresponds to the maximum extension of the H $\alpha$  line formation region in dense enough winds such as those of O supergiants. Evidently, these clumps can coexist with the large-scale perturbations (DACs) observed in the UV domain.

For our modeling, we assumed that the clumping properties of the wind are determined by small-scale structures that originate from the intrinsic instability of the line-driving mechanism. Hence, the derived clumping properties should be (almost) independent of time, as long as the major wind characteristics remain

largely constant. This is supported by observations that on longer time scales, the wind properties of most O stars appear to be constant. Additional support comes from a study showing that for early-type supergiants, variations observed in H $\alpha$  indicate mass-loss rate changes of about  $\pm 4\%$  with respect to the mean value of  $\dot{M}$  (Markova et al. 2005). These changes are smaller than the uncertainties of our  $\dot{M}$  estimates, most of which are attributable to uncertainties in the stellar luminosities.

### 3. Model atmospheres

We performed the analyses using model atmospheres calculated with the code CMFGEN (Hillier & Miller 1998). This code computes line-blanketed, non-LTE (NLTE) models by solving the radiative transfer and statistical equilibrium equations in the co-moving frame of the fluid, for a spherically symmetric outflow. To help facilitate the inclusion of line blanketing, super-levels were used. This approach allows the inclusion of many energy levels from ions of many different species. After convergence of the model, a formal solution of the radiative transfer equation is computed in the observer’s frame (Busche & Hillier 2005), thus providing the synthetic spectrum for comparison to observations.

For the photospheric density structure we initially used the hydrostatic density structure for a model computed with TLUSTY (Hubeny & Lanz 1995; Lanz & Hubeny 2003), while for the wind we used a standard  $\beta$ -velocity law that is connected to the hydrostatic density structure just above the sonic point (at approximately 15 km s<sup>-1</sup>). The mass-loss rate, density, and velocity are related via the continuity equation. In more advanced models we iterated on the density structure so that the hydrostatic equation,

$$dP/dr = -g_{\text{grav}} + g_{\text{rad}} \quad (1)$$

where

$$g_{\text{grav}} = GM/r^2 \quad (2)$$

and the radiative acceleration  $g_{\text{rad}}$

$$g_{\text{rad}} = \frac{4\pi}{c} \rho \int \chi_{\nu} H_{\nu} d\nu \quad (3)$$

was satisfied. We solved for the density structure by integrating the hydrostatic equation using the Runge-Kutta method. To facilitate the integration, the Rosseland LTE opacity was computed as a function of temperature and electron number density for the model abundances prior to the CMFGEN run. In a typical CMFGEN model, a hydrostatic iteration is performed after

the first model iteration and then every  $n$  (with  $n \sim 8$ ) iterations. Generally 3 to 4 hydrostatic iterations are needed to obtain convergence to better than 5% everywhere.

A depth-independent microturbulent velocity is included in the computation of the atmospheric structure (i.e., temperature and level populations). A value of  $15 \text{ km s}^{-1}$  is adopted as the default in our computations.

We have computed clumped wind models with CMFGEN. Clumping is implemented through a parameteric, volume filling-factor approach, which assumes that the clumps are optically thin to radiation and the inter-clump medium is void. Under these assumptions, the clumped wind density,  $\rho(r)$  is related to the homogeneous (unclumped) wind density and the volume filling by  $\rho(r) = \bar{\rho}/f$ . The filling factor decreases exponentially with increasing radius (or, equivalently, with increasing velocity):  $f = f_\infty + (1 - f_\infty) \exp(-v/v_{cl})$  where  $v_{cl}$  is the velocity at which clumping starts. We tuned  $v_{cl}$  to improve the fit to some observed lines (Bouret et al. 2005). A limitation of this parameterization is that  $f$  is monotonic whereas theoretical simulations by Runacres & Owocki (2002) and observational studies (Puls et al. 2006; Najarro et al. 2011) suggest it is non-monotonic.

We have accounted for shock-generated X-ray emission in our models<sup>2</sup>. An important consequence of the X-ray and EUV shock radiation is enhanced photoionization which results in “wind super-ionization” — that is the presence of highly ionized ions (such as O VI) that are not expected to be produced by the photospheric radiation field. These super-ions are primarily produced by the Auger process (Cassinelli & Olson 1979). In this process a X-ray photon causes the ejection of an inner shell electron from an ion. The ion, which is in a highly excited state, usually autoionizes. For CNO elements, the net change in the charge of the X-ray-absorbing ion is generally +2. Auger processes, and direct ionization by the shock radiation field, are accounted for in calculating the wind ionization. Only two stars in our sample have been observed with X-ray satellites, namely  $\zeta$  Puppis and  $\lambda$  Cep with *ROSAT*; the X-ray luminosities are  $\log L_X = 32.43$  and  $\log L_X = 31.92$ , respectively (see Oskinova 2005). The luminosity ratios,  $\log L_X/L_{bol}$ , for these stars were computed using the bolometric luminosities as determined from this study. For HD 190429A, HD 14947, HD 15570 and HD 16691, we have adopted the X-ray luminosity of  $\zeta$  Puppis, while the X-ray luminosity of  $\lambda$  Cep was chosen as a proxy for HD 163758 and HD 192639.

## 4. Diagnosing stellar and wind parameters

### 4.1. Stellar luminosity

The stellar luminosity  $L$  is one of the key input parameters to CMFGEN. It is usually derived from the absolute magnitude, which requires accurate knowledge of the distance of a star.

Because HD 15570 is a member of the cluster IC1805, we adopted the distance modulus of the cluster (Massey et al. 1995),  $DM = 11.85 \pm 0.1$  (which corresponds to a distance of 2.3 kpc), to derive  $M_V$ , hence  $L$ . A significant absorption is also present toward this cluster, which translates into a fairly high reddening of the stellar spectra. Remarkably, the color excess we derive from fitting the observed SED differs by less than 1% from the  $E(B - V)$  computed from observed (B-V) and theoretical (B-V)<sub>0</sub> from Martins & Plez (2006).

<sup>2</sup> In these stars the clumps are probably primarily responsible for producing the observed N v resonance doublet, but in cooler stars the inter-clump medium is also likely to be very important (Zsargó et al. 2008)

For all other stars, the distance is poorly known, with sometimes fairly large differences in estimates of the distance modulus. This leads to significant uncertainties in the luminosity, which in turn translates into differences in some parameters such as the mass and the mass-loss rate, which depend on the stellar luminosity through the implied value of the stellar radius (see, e.g., Puls et al. 1996). We adopted the following procedure:

1. We adopted an initial absolute magnitude (and corresponding distance) for each object from the literature. We used  $M_V$  values listed in Markova et al. (2004) for HD 14947, HD 16691,  $\zeta$  Puppis, HD 192639 and  $\lambda$  Cep, while  $M_V$  was taken from Repolust et al. (2005) for HD 190429A. For HD 163758, we found no  $M_V$  listed in the literature and we adopted  $M_V$  from the calibration by Martins & Plez (2006). From  $M_V$ , we derived  $L$  assuming a bolometric correction from Martins et al. (2005). We then searched for the model that best fits the normalized UV and optical spectra. This model yields the photospheric and wind parameters. We derived  $\dot{M}$  by requiring that the model fits H $\alpha$ . Any value of  $\dot{M}$  and  $R_*$  such that  $\dot{M}/R_*^{1.5}$  is constant provides a similar fit to H $\alpha$  (and He II  $\lambda 4686$ ). However, UV lines do not follow the same trend, and this allowed us to break the degeneracy between  $\dot{M}$  and  $R_*$  to some extent..
2. From the best-fit model, we fitted the flux calibrated *IUE* spectra and UBVJHK fluxes (for the photometry see Table 1) to constrain the distance and the extinction. The Galactic reddening law of Cardelli et al. (1989) was used. We varied the distance (global scaling) and color excess  $E(B - V)$  (wavelength-dependent leverage) to reproduce the UV-optical-near-infrared spectral energy distribution (SED).
3. The absolute magnitude  $M_V$  was recomputed with the distance derived in step 2 from the fit to the observed fluxes. If the new value differed from the value initially assumed in step 1 by 0.05 dex or more, it was used to compute a new luminosity and a new model atmosphere. When the revised model atmosphere is calculated,  $T_{\text{eff}}$ ,  $\log g$ ,  $v_\infty$ ,  $\beta$  and the abundances were kept fixed to their respective values derived in step 1, but  $\dot{M}$  and  $f$  (the clumping filling factor) were varied to determine a new best fit to the normalized spectra.
4. This set of three steps was repeated until we converged on a solution satisfying both the fit to the individual spectral wind features from the normalized spectra and the absolute UV + optical/near-IR (NIR) fluxes.

Final values for the distances and absolute magnitudes are listed in Table 1. The SEDs for each star resulting from the process above are presented in Fig. 1.

### 4.2. Effective temperature, $\log g$ and helium abundance

Our primary  $T_{\text{eff}}$  diagnostics in the optical were the ratio of He I  $\lambda 4471$  to He II  $\lambda 4542$  equivalent widths, as well as line profile fitting. We used the other lines of He I and He II to refine the  $T_{\text{eff}}$  determination. The optical helium lines were also used to constrain the relative He to H abundance. In addition to these classical helium diagnostics, we also used metal lines for estimating the effective temperature. This is particularly relevant for the earliest stars of the sample, which have weak He I lines, and for which the validity of using the helium ionization balance to determine  $T_{\text{eff}}$  accurately is questionable. In the UV the Fe IV to Fe V and Fe V to Fe VI ionization ratios provide a sensitive temperature diagnostic. We found consistent estimates with the helium ion ratios within one thousand Kelvin for most objects, a slightly higher difference for  $\zeta$  Puppis and  $\lambda$  Cep is related to

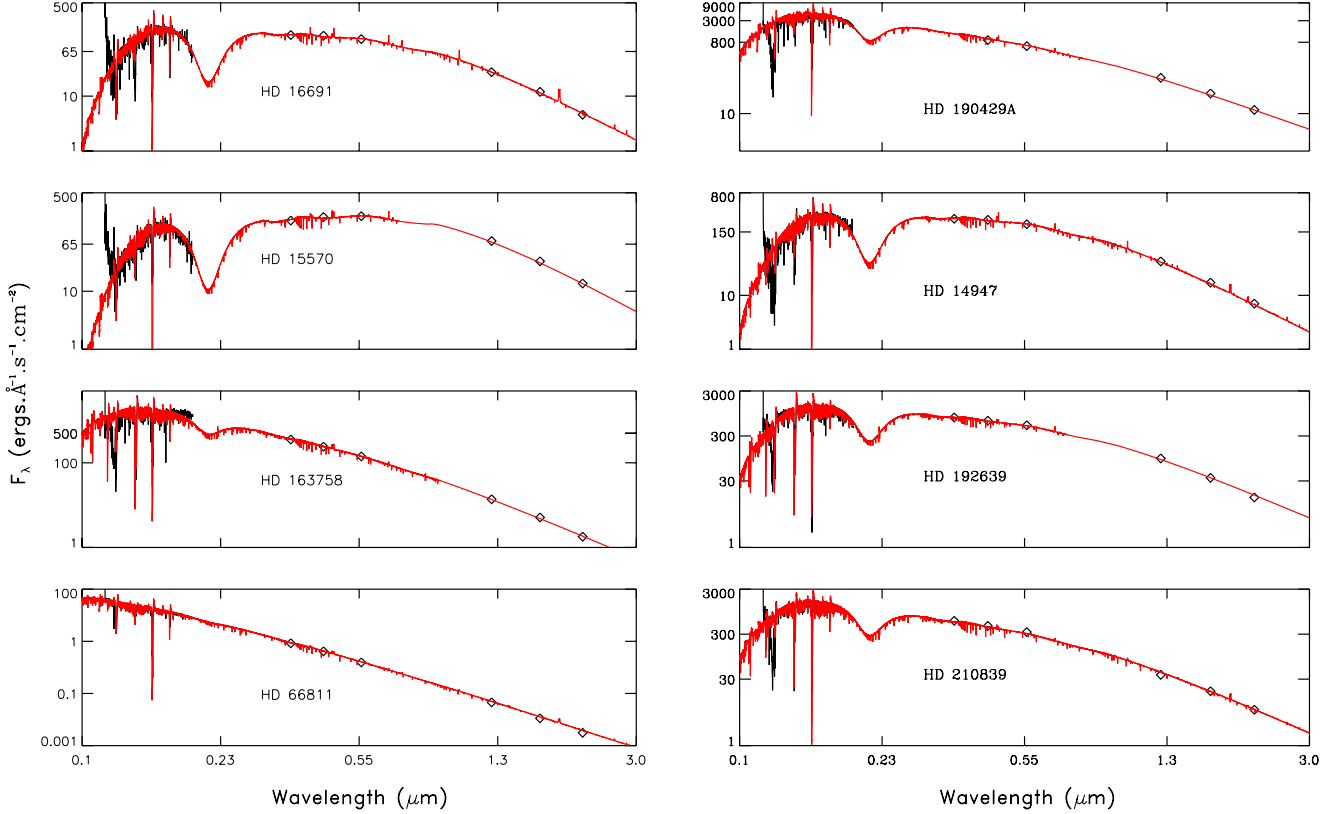


**Fig. 1.** Synthetic SEDs (in red) compared to flux calibrated + UBVJHK photometry for the target stars (in black). The distance, E(B-V) and luminosity were iterated to reach agreement between models and observations (see Sect. 4.1). For plotting purpose, the fluxes were scaled by a factor  $10^{14}$  for all stars but HD 66811 and HD 210839, where factors  $10^9$  and  $10^{13}$  were used, respectively.

the higher  $v \sin i$  of these objects. When possible (HD 190429A and HD 16691), we also used the C iv  $\lambda 1169$  to C iii  $\lambda 1176$  line ratio which has also been shown to provide a useful temperature diagnostic by Heap et al. (2006).

In some cases, effective temperature determinations based on the ionization ratio of optical helium lines are inconsistent with some temperature-sensitive metal lines, such as N v  $\lambda\lambda 4605$ -4620. The presence of these lines in the observed spectra points to an enhancement in  $T_{\text{eff}}$  of approximately 2000 K compared to the values derived from the helium lines. The relative strength of the N v doublet, which is strongly dependent on the temperature, has a relatively weak dependence on gravity, while the absolute strength was better reproduced by tuning the nitrogen abundance. Nevertheless, we could not achieve a good fit to these lines without degrading the agreement with the rest of the optical and UV spectrum. The values of  $T_{\text{eff}}$  and nitrogen abundance needed to fit these lines should be regarded as upper limits.

The Stark-broadened wings of H $\gamma$  provided the primary constraint on  $\log g$  (other Balmer lines were used as secondary indicators). The typical uncertainty in  $\log g$  is 0.1 dex. Despite the high S/N of our spectra it is difficult to do better than this —  $\log g$  has to be determined simultaneously with  $T_{\text{eff}}$ , and there are slight inconsistencies with different lines (because of rectification errors and residual uncertainties with the atomic physics).

#### 4.3. Micro-turbulence

The formal solution of the equation of transfer was used with a radially dependent turbulent velocity to calculate the emergent spectrum (see also Hillier & Miller 1998). In this case, the mi-

cro-turbulent velocity follows the relation  $\xi_t(r) = \xi_t^{\text{min}} + (\xi_t^{\text{max}} - \xi_t^{\text{min}}) \frac{v(r)}{v_{\text{mf}}}$  where  $\xi_t^{\text{min}}$  and  $\xi_t^{\text{max}}$  are the minimum and maximum micro-turbulent velocities. The microturbulence at the photosphere is chosen to best reproduce the strength of the S v  $\lambda 1502$  and iron lines (Fe iv and Fe v) in the IUE spectra. The adopted  $v_{\text{turb}}$  has little effect on the strength of most H i lines. On the other hand, we found some significant changes for important  $T_{\text{eff}}$  diagnostics such as He i  $\lambda 4471$  and some He ii lines (see also Villamariz & Herrero 2000). We confirm findings by Hillier et al. (2003) that He ii  $\lambda 5411$  is also sensitive to the microturbulent velocity, while He ii  $\lambda 4541$  or He ii  $\lambda 4686$  are not.

In the outer region of the wind, the turbulence is adopted to best fit the shape and slope of the blue side of the absorption component of the C iv  $\lambda\lambda 1548$ -1551 P Cygni profile.

#### 4.4. Surface abundance

Accurate CNO abundances provide key constraints on both the evolutionary state and the influence of rotation, and should preferably be determined from photospheric lines of these elements.

We adopted the solar abundances from Asplund et al. (2005) as a reference. The new values better agree with surface abundances of B-type stars in the solar neighborhood (see Cunha et al. 2006; Przybilla et al. 2008; Simón-Díaz 2010; Nieva & Simón-Díaz 2011). Some caution may be required when comparing these baseline abundances to those we derive since only one star ( $\zeta$  Puppis) is located within 1 kpc, which is the limit usually set for solar neighborhood abundance studies (but see the recent work by Nieva & Przybilla 2012).

#### 4.4.1. Carbon abundance

Most carbon lines in the FUV/UV range suffer from wind contamination and we chose not to use them as prime indicators for carbon abundances. For stars with  $T_{\text{eff}} \leq 35,000$  K, C III  $\lambda 1247$  appears as an emission line with a clear response to abundance variations. This is the only diagnostic for carbon abundance in the UV for these stars.

In the optical, available lines depend on the temperature range (except for C IV  $\lambda 5801$ -5812 which are present for all stars). In a few stars, C III  $\lambda 4647$ -50-52 lines are clearly detected and were used. For stars cooler than 38,000 K, C III  $\lambda 5696$  was used. For stars with  $T_{\text{eff}} \leq 35,000$  K, C III  $\lambda 4068$  is present as a non-saturated absorption line and was also used to measure the carbon abundance. Finally, we checked for consistency with the other C III diagnostics listed above using the C III emission lines at  $\lambda 6721$ , C III  $\lambda 6727$ -6730.

#### 4.4.2. Nitrogen abundance

In the UV, the photospheric lines of N III  $\lambda 1748$ -1752 were used. However, these features saturate when the nitrogen abundance exceeds about five times the solar value, at which point they are no longer useful abundance diagnostics.

In the optical, N III  $\lambda 4379$ , N III  $\lambda 4634$ -4640-42, N III  $\lambda 4510$ -4515, N III  $\lambda 5320$ -5327, N IV  $\lambda 5204$ -5205, N IV  $\lambda 6380$ , N V  $\lambda 4944$  and N IV  $\lambda 6212$ -6220 are available. We furthermore used the emission lines of N V  $\lambda 6716$ -6718 to check for consistency only, because these lines are often blended with C III lines ( $\lambda 6721$ ,  $\lambda 6727$ -6730).

We found that the N IV  $\lambda 5205$  line provided the most reliable abundances in optical spectra of O4 – O5 supergiants. It is sensitive to abundance changes, with no sign of saturation within the limits we tried. While there may be problems with the absolute calibration of abundances based on this line, relative abundances should be much more accurate.

#### 4.4.3. Oxygen abundance

The O III  $\lambda 5592$  line provides the best constraint on the oxygen abundance in optical spectra. Indeed, this line is not contaminated by wind contribution and is observed as an absorption line (though often weak), in a region of the spectrum where the continuum is well defined. We also used the O III triplet ( $\lambda 1150$ -1154 Å) in the *FUSE* spectrum, when fast rotation does not blend them with other metal lines. UV lines (O IV  $\lambda 1338$ -1343 and O V  $\lambda 1371$ ) indicate a (sometime significant) contribution from the wind and were not used.

#### 4.4.4. Formation of some specific lines

Before proceeding further it is worth making some general comments about photospheric lines, which sometimes appear in emission in O stars. If we assume the Eddington-Barbier relation holds, these transitions are in emission because the source function is larger than the neighboring continuum source function. This can occur because the population of the upper level is enhanced, or because the population of the lower level is depleted. Many of the transitions occur between the  $n=3$  levels of CNO ions ( $n=4$  for Si IV), and involve one, or more levels, coupled to low-lying levels by transitions in the EUV (i.e., shortwards of 900 Å). Depending on the EUV radiation field, these transitions can drain or populate a particular level. These transitions

can also be influenced by overlapping lines from other species (e.g. Najarro et al. 2006), and by the adopted abundances (which directly alters the optical depth of the line). In CNO elements, dielectronic recombination may play a role by selectively enhancing the populations of some levels relative to others (Rivero González et al. 2011).

In WN stars, Hillier (1988) found that the strong N IV emission lines (4058 Å, 3478-3485 Å, 7013-7129 Å) are influenced by continuum fluorescence and dielectronic recombination. The C IV  $\lambda 5801$ -5812 doublet is also strongly influenced by continuum fluorescence, which is pumped by a transition at 312 Å. On the other hand, in WC stars, with their large carbon mass-fraction ( $> 0.1$ ), radiative and dielectronic recombination dominate the formation of optical carbon lines (Hillier 1989). For O stars the situation is likely to be more complicated (the densities are higher and more processes are likely to be important) because LTE must be recovered close to the line formation region. Fits to these lines significantly improved when we computed models with a much larger number of atomic elements, which were originally included to improve the calculation of the line radiative force. We found that the change induced in the total EUV line-blanketing yielded C IV  $\lambda 5801$ -5812 profiles that better agreed with observations.

C III  $\lambda 4647$ -50-52 lines form very near the stellar surface and are marginally sensitive to wind parameters. In addition, the lower level of C III  $\lambda 4647$ -50-52 ( $1s^2 2s 3s - 1s^2 2s 3p$ ) corresponds to the upper level of C III transitions around 538 Å ( $1s^2 2s 2p - 1s^2 2s 3s$ ). Around this wavelength, Fe IV lines are present and overlap with the C III line. These Fe IV lines drain and depopulate the lower level of the C III  $\lambda 4647$ -50 transition (see also Martins & Hillier 2012, in preparation). We had to reduce significantly the oscillator strengths of Fe IV lines around 538 Å to obtain satisfactory fits to these C III lines. This sensitivity to atomic model assumptions must be kept in mind when using these lines for abundance determinations.

C III  $\lambda 5696$  requires many energy levels in our model atom to form in emission as observed. However, in some cases we could not reach a satisfactory fit of the lines, indicating that some mechanism or process that is affecting the formation of this line has not been correctly accounted for in our modeling. To our knowledge, systematic studies of the formation of C III emission lines have been performed for WC stars only. We note first that C III  $\lambda 5696$  behaves differently from other C III emission lines, even though it varies smoothly along the WC spectral sequence, (e.g. Torres et al. 1986). C III lines such as  $\lambda 2296$  and C III  $\lambda 6741$  are strong in WC4 stars, while  $\lambda 5696$  is very weak or absent. On the other hand, in late WC stars,  $\lambda 5696$  is the strongest optical C III transition. This behavior occurs because the upper level of  $\lambda 5696$  ( $2s 3d \ ^1D$ ) can also decay to the  $2s 2p \ ^1P^o$  via a transition at 574 Å — only when the transition is optically thick will  $\lambda 5696$  be strongly in emission ( $A(\lambda 574)/A(\lambda 5696)=150$ , Storey [private communication]) (Hillier 1989). The lower level is coupled to the  $2p^2 \ ^1D$  state by a transition at 884 Å, highlighting the importance of EUV transitions on the source function for the  $\lambda 5696$  transition. Note that  $\lambda 4058$  is the N IV isoelectronic equivalent transition to C III  $\lambda 5696$ .

Mihalas et al. (1972) showed that the N III  $\lambda 4643$ -4640-4642 feature can be driven into emission by dielectronic recombination, and highlighted the importance of two-electron transition for draining the  $3p$  state. They also noted that the Swings mechanism (i.e., continuum fluorescence) could be important in stars with winds. Very recently, Rivero González et al. (2011) showed that in stars with stellar winds, the Swings mechanism



is indeed more important, although they also note that in O stars cooler than 35,000 K the interaction between the O III and N III resonance lines could also be important.

N IV  $\lambda\lambda 6212-6220$  ( $2s 4^3S - 2s 4p^3P^o$ ) appears as an emission feature in the earlier supergiants. Our original models failed to reproduce this line, which was traced to a problem with the theoretical model atom. In the atomic data calculations the levels designations of the  $2s 4s^3S^o$  with the  $2p 3p^3P^o$  level (as previously noted by Laughlin 1990; Allard et al. 1991) are inverted relative to the spectroscopic designations. When we rectified this inversion, emission in N IV  $\lambda\lambda 6212-6220$  was correctly reproduced.

In our models for some of the O4 supergiants, the N IV  $\lambda 4058$  line shows up as an intense emission feature, which is not observed. The N V  $\lambda\lambda 4605-4620$  lines are present as photospheric absorptions in O4 supergiant spectra only. Since they are also very sensitive to effective temperature we did not use them to constrain the nitrogen abundance. Walborn (2001) describes an apparent connection between the N V  $\lambda\lambda 4605-4620$  and the N IV  $\lambda 4058$  lines: the former appear in absorption in early-type supergiants, while the latter are seen in emission of “similar inverse intensity”. Although the presence and relative intensity of these lines is clearly defined in Of supergiants, there is no obvious physical connection that would explain their observed proportionality (other than they both depend on  $T_{\text{eff}}$ ).

#### 4.5. Wind parameters

The wind terminal velocities,  $v_{\infty}$ , were estimated from the blueward extension of the absorption part of UV P-Cygni profiles, which occurs up to  $v_{\infty} + v_{\text{max}}$ , where  $v_{\text{max}}$  is the maximum microturbulent velocity described above. Fits of the UV P-Cygni profiles using the above relation for microturbulent velocity allows a direct determination of  $v_{\infty}$ . The typical uncertainty in our determination of  $v_{\infty}$  is  $100 \text{ km s}^{-1}$  (depending on the maximum microturbulent velocity we adopt).

Mass-loss rates are derived from the simultaneous analysis of strong UV lines such as C IV  $\lambda\lambda 1169 + 1176$ , N V  $\lambda\lambda 1240$ , C IV  $\lambda\lambda 1548, 1551$ , Si IV  $\lambda\lambda 1394, 1403$ , O V  $\lambda 1371$  and N IV  $\lambda 1718$ . In the optical the strength of H $\alpha$  and He II  $\lambda 4686$  is sensitive to  $\dot{M}$ , while the shape of their emission profile is sensitive to the  $\beta$  exponent of the wind velocity law.

Following Bouret et al. (2005), clumping-related quantities ( $\dot{M}$ ,  $f_{\infty}$  and  $v_{\text{cl}}$ ) were derived from P V  $\lambda\lambda 1118, 1128$ , O V  $\lambda 1371$ , and N IV  $\lambda 1718$  in the FUV/UV domain, to which we added clumping sensitive lines from the optical, primarily H $\alpha$  and He II  $\lambda 4686$ . We emphasize here that some photospheric lines in the UV and optical are also sensitive to the adopted filling factor (and scaled  $\dot{M}$ ). For photospheric H I and He lines for instance, this is essentially caused by a weaker wind contribution (emission) in clumped models, which produces deeper absorption compared to smooth-wind models. For a more detailed discussion concerning the sensitivity of line to the wind and clumping, see Hillier et al. (2003).

## 5. Results of the spectroscopic analysis

The synthetic spectra were convolved with a representative instrumental profile and a rotational profile calculated for a trial value of the projected rotational velocity ( $v \sin i$ ) to permit direct comparison with observations. We varied  $v \sin i$  until we achieved a good fit to the observed photospheric profiles.

As an independent check, we used the Fourier transform method described in Simón-Díaz & Herrero (2007, and reference therein) to determine  $v \sin i$  from the observed spectra.

To apply the Fourier transform method, we selected lines with as weak a wind contribution and as symmetric a profile as possible. We identified several isolated photospheric lines (which included N V  $\lambda\lambda 4604 - 4620$  for HD 190429A and  $\zeta$  Puppis, O III  $\lambda 5592$  for cooler stars), which we used to derive individual values that we averaged to yield the values listed in Table 3. For the fast rotators, namely  $\zeta$  Puppis and  $\lambda$  Cep,  $v \sin i$  from the two methods agree better than within  $10 \text{ km s}^{-1}$ , which is well within the typical error bars of each method. For the other moderately rotating stars, the difference is smaller than  $20 \text{ km s}^{-1}$ , which is slightly smaller than the difference found for other O-type supergiants by Simón-Díaz & Herrero (2007). The final values used in our models are listed in Table 3.

The quality of the fits was then additionally improved by convolving the rotationally broadened profiles with a Gaussian of FWHM  $v_{\text{mac}}$  to account for (isotropic) macro-turbulence. More complex description of the macro-turbulence exists, e.g. the so-called radial-tangential broadening. In the specific case of massive stars, Aerts et al. (2009) recently interpreted the missing line broadening in terms of the collective effect of numerous, low-amplitude, non-radial gravity-mode oscillations. These authors emphasized that using the Gaussian formulation of macro-turbulence to fit line profiles could lead to significant underestimation of the actual rotational velocity and warned that appropriate expression for the pulsational velocities should be used instead. Therefore, the values quoted in Table 3 should be regarded as lower limits, but we do not expect significant modifications of our conclusions concerning surface abundances. First, rotation and macro-turbulence in the adopted description are not expected to affect line equivalent widths, only the line profiles (contrary to micro-turbulence). Second, differences between rotational broadening from line fitting, which should be regarded as an upper limit, or from Fourier transform are quite small (less than  $20 \text{ km s}^{-1}$ , see above). Third, in the total broadening we considered, the rotational term is always dominant with respect to macro-turbulence.

Given the complexity of the fitting process over the FUV to optical spectral range, we chose not to derive formal statistical uncertainties, nor did we try to estimate the correlation of errors between parameters. Instead, we varied the different parameters until we obtained the solution that provided the best fit by eye to the observations, with more weight being given to primary diagnostics (cf Sect. 4). Then, for a more quantitative estimate, we varied each parameter independently around this solution and computed the residual (i.e. the difference) between the observed and the synthetic spectrum. We imposed the condition that this residual must remain within  $\pm 10\%$  and adopted the range of values that fulfilled this condition as error bars on each parameter. The stellar and wind parameters we derived are gathered in Table 3. We quote all chemical abundances by number and mass fraction, except for He I, which is given by number relative to hydrogen (see Table 4). As for the uncertainty in the CNO abundance measurements, error bars are based on the fit quality of the lines listed above, as estimated from a classical  $\chi^2$  procedure. Our conclusions for individual objects are summarized in the remainder of the section. The best-model fits to the data are presented in Appendix A.



### 5.1. HD 190429A - O4 If

HD 190429A was studied extensively in the UV in Bouret et al. (2005). We recomputed their best-fit model, using the new Asplund et al. (2005) abundances. We scaled the CNO as well as P and S abundances to the same relative values as in Bouret et al. (2005). The best fit to the P v  $\lambda\lambda 1118-1128$  resonance doublet is obtained for  $P/P_{\odot} = 0.7$ , further confirming the *apparent* depletion in phosphorus of this star. Only a limited tuning of the model parameters was needed to improve the fit to the optical lines, which demonstrates the reliability of our FUV/UV analysis. The best fit to FUV-UV and optical spectra is presented in Appendix A. Note however that the presence of strong lines of N v  $\lambda\lambda 4605-4620$  would require significantly higher temperature to be reproduced ( $T_{\text{eff}} \approx 43,000$  K), which would then make the fit worse everywhere else in the spectrum (see also comments on Sect. 4.2).

The C III  $\lambda\lambda 4647-50-52$  lines are weak, especially compared to the strong neighboring N III  $\lambda\lambda 4634-4640-4642$  lines. This was recognized (e.g. by Walborn et al. 2010) as due to an abundance effect, as CNO processed material is expected at the surface in supergiants. We found that the atmosphere of HD 190429A is highly depleted in carbon ( $X(\text{C}) = 0.009\%$  by mass), and is enriched in nitrogen ( $X(\text{N}) = 0.73\%$ ). Although derived from fewer lines, the oxygen abundance corresponds to a mass-fraction  $X(\text{O}) = 0.067\%$ . Together with the He enrichment  $y = 0.2$ , this is qualitatively consistent with the general trend predicted by evolutionary models with rotation.

### 5.2. $\zeta$ Puppis - O4 I(n)fp

Although a model with  $T_{\text{eff}} = 39,000$  K provides an excellent fit to helium lines, raising  $T_{\text{eff}}$  up to  $41,000$  K better agrees with the observed N v  $\lambda\lambda 4605-4620$  lines, which are otherwise too weak. Deriving the actual value proved to be elusive, but we expect that  $T_{\text{eff}} = 40,000 \pm 1000$  K is a realistic estimate of the effective temperature of  $\zeta$  Puppis. The wind properties agree very well with those presented in Najarro et al. (2011) based on the modeling of the near-infrared spectrum of  $\zeta$  Puppis. Only clumped-wind models matched the whole set of wind-sensitive lines. The best fit to P v  $\lambda\lambda 1118-1128$  lines was nevertheless obtained only when using sub-solar phosphorus abundance,  $P/P_{\odot} = 0.5$ . We needed to start clumping at  $v_{\text{cl}} = 100$  km s<sup>-1</sup>, significantly above the sonic point to obtain a reasonable fit of the central trough of H $\alpha$ . This indicates that more absorption is needed in the line formation region, which is missing if clumping starts right above the photosphere. It is remarkable that this behavior is observed on the other fast rotator of our sample  $\lambda$  Cep, as well as in HD 16691, whose emission lines present strong similarities with those of  $\zeta$  Puppis (see below): N III  $\lambda\lambda 4634-4640-4642$  presents a box-shaped profile, while He II  $\lambda 4686$  is clearly double-peaked. Based on preliminary models using a realistic 2D treatment of rotation as described in Busche & Hillier (2005) and Zsargó et al. (2006), we concluded that the shapes of these emission lines are most easily interpreted in terms of an effect of high rotational velocity. These conclusions will be presented in a forthcoming paper.

Despite the high  $v \sin i$  of this star, many lines of CNO ions are present in the spectra to derive reliable estimates of the surface abundances (see Fig. A.4). One such line worth mentioning is the N IV  $\lambda\lambda 7103-7129$  multiplet, which is the triplet equivalent of N IV  $\lambda 4058$ . Our FEROS spectrum of  $\zeta$  Puppis shows an emission feature at these wavelengths whose strength is very sensitive to abundance variations and is well-matched in our fi-

nal model. The total of CNO abundances is clearly super-solar in  $\zeta$  Puppis (see Table 4). It has been argued that this could be the result of a binary/merger evolution (Pauldrach et al. 2012), in line with the runaway status often invoked for this star (Sahu & Blaauw 1993). We stress, however, that in Pauldrach et al. (2012), this conclusion is based on abundances for several elements, which are very different from what we derive. Their high C abundance for instance seems impossible to reconcile with the observed optical spectrum when modeled with CMFGEN. Detailed comparisons between the two analyses are needed to elucidate this problem.

We also note that the luminosity we adopted differs significantly from those quoted in Najarro et al. (2011) or Pauldrach et al. (2012). These two studies chose the higher value, often related to its runaway status, while we adopted a lower value for the distance, compatible with the *Hipparcos* distance quoted for  $\zeta$  Puppis. On the other hand, Schilbach & Röser (2008) found  $\zeta$  Puppis to be even closer (300 pc) than given by *Hipparcos* (430 pc). These authors suggested that the star originally was in the open cluster Trumpler 10, which it left about 2.5 Myrs ago. A direct consequence of this lower distance would be to revise the luminosity downward to  $\log L/L_{\odot} = 5.42$ . The stellar mass would go down accordingly ( $\approx 17 M_{\odot}$ ), which starkly contradicts the usual parameters of an O4 supergiant.

### 5.3. HD 16691 - O4 If

A model with  $T_{\text{eff}} = 41,000$  K  $\pm$  1000 K best fits the He lines as well as N v  $\lambda\lambda 4605-4620$  in HD 16691. Carbon lines in the optical are weak, which suggests a high depletion of this element (but see Sect. 4.4 for comments about the sensitivity of C IV  $\lambda\lambda 5801-5812$  doublet to the treatment of UV blanketing). This is also supported by the C IV  $\lambda 1169$  and C III  $\lambda 1176$  lines, which show up as weak absorptions. Nitrogen lines are strong, indicating that this element is altogether highly enriched. We note that despite several tests we performed, N IV  $\lambda 4058$  is predicted to be strongly in emission compared to the observed profile. Fitting this line would require a much lower nitrogen abundance, inconsistent with the rest of the nitrogen lines. In accordance with its Of/WN transition status (Conti & Bohannan 1989), HD 16691 furthermore presents a clear enrichment in He.

Only clumped models agree well with the observed wind sensitive lines. The best fit to P v  $\lambda\lambda 1118-1128$  lines was obtained using sub-solar phosphorus abundance  $P/P_{\odot} = 0.5$ .

UV and optical spectra of HD 16691 and HD 190429A show strong similarities, reminiscent of those seen in their IR *K*-band spectra (e.g. the subordinate He II  $2.189\mu\text{m}$  in emission). Conti et al. (1995) noted that both stars would have been classified as WN stars had they been observed only in the *K*-band. These spectral similarities strongly suggest a common evolutionary status for these objects.

HD 16691 and  $\zeta$  Puppis also share some striking similarities (see Table 3), especially regarding the emission lines of their optical spectra, such as N III  $\lambda\lambda 4634-4640-4642$  and He II  $\lambda 4686$ . We argue that a high rotation rate is able to explain the observed emission profiles of HD 16691, and there is no need to invoke an extended corotating region that would be caused by a putative magnetic field, as proposed by De Becker et al. (2009). Furthermore, we needed to start clumping at  $v_{\text{cl}} = 130$  km s<sup>-1</sup> in our models to best reproduce the observed spectra. This behavior is again very reminiscent of that of the other fast rotators of our sample (see below) and might indicate that the wind of HD 16691 is indeed rotating faster than suggested from the photospheric lines.

#### 5.4. HD 15570 - O4 If

HD 15570 is one of the brightest early-type stars in the young open cluster IC 1805. The FUV-UV spectra are heavily masked by interstellar absorption lines (mostly  $H_2$  in the *FUSE* spectrum), consistent with the large  $E(B - V)$  we derive (see Sect 4.1). The microturbulent velocity, which is usually best determined from  $S\ v\ \lambda 1502$  and the iron line strengths (Fe IV and Fe V) could not be accurately measured and we used optical lines only, to derive a value  $\xi_t = 15\ \text{km s}^{-1}$ .

We derived  $T_{\text{eff}} = 38,000\ \text{K}$ ,  $\log L/L_{\odot} = 5.94$  for HD 15570, which implies that it is somewhat cooler than expected for its spectral type, although at the expected luminosity according to Martins et al. (2005). Usually the observed differences/dispersion in this calibration can account for a large part of the uncertainty in the luminosity, i.e., the distance to this object. This should not be the case for HD 15570 because the distance modulus IC1805 cluster is well determined.

More puzzling, the He lines of HD 15570 are weak for its spectral type. Since the photospheric and wind parameters of HD 15570 (see Table 3) are very close to those of HD 190429A, we compared the optical spectra of both stars. The unusually weak helium lines of HD 15570 are clearly apparent in Fig. 2, where He lines are stronger and broader in HD 190429A ( $v \sin i$  for HD 190429A is higher than for HD 15570).

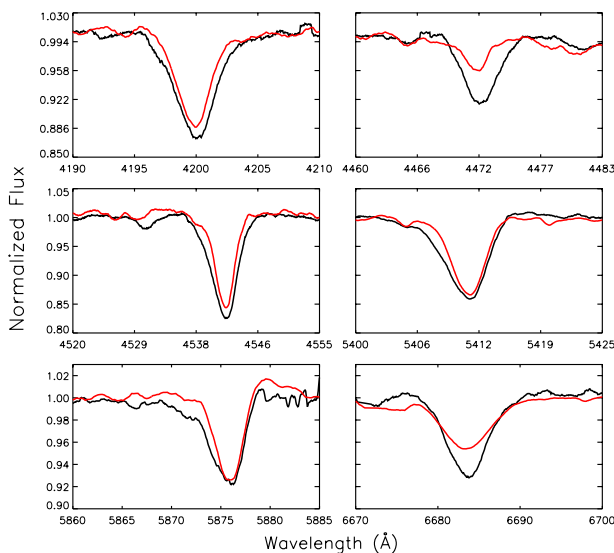


**Fig. 2.** Helium line profiles from the optical spectra of HD 190429A (black) and HD 15570 (red). HD 190429A has  $v \sin i = 150\ \text{km s}^{-1}$ , while it is  $97\ \text{km s}^{-1}$  for HD 15570.

The high-resolution spectrum of HD 15570 presented in De Becker et al. (2006)<sup>3</sup> was kindly provided to us by G. Rauw for comparison to our spectrum. Both spectra are remarkably similar throughout the common spectral range (4000 - 6800 Å), including the weak and narrow(er) helium lines with respect to the star's photospheric properties. This confirms that our finding is not an observational artifact caused by incorrect data reduction or spectrum rectification. Spectra retrieved from the *ELODIE* archives<sup>4</sup>, which cover the epoch from 1996 to 2005 and have

<sup>3</sup> Obtained with the echelle spectrograph at the 2.1 m telescope at the Observatorio Astronómico Nacional de San Pedro Martir (SPM) in Mexico

<sup>4</sup> <http://atlas.obs-hp.fr/elodie/>

a signal-to-noise ratio of 100 or higher, also display the same narrower, weaker helium lines. This confirms that the weakness of He lines is not time-dependent, at least on this timescale.

Quantitatively, we found that  $y(\text{He}/\text{H}) = 0.07$  (by number) is needed to best fit the helium lines in the optical domain. Such a low He abundance is not supported by stellar evolution considerations, but we could not find any problems with the observations that would affect the analysis of He lines. It is unlikely that this lower helium abundance is an indication of the initial composition of the molecular cloud from which HD 15570 formed. Martins et al. (2005) found  $y = 0.1$  for HD 15629, a main-sequence O5V((f)) star in IC 1805, which suggests that the initial helium content of this cluster is normal. In the rest of this work, we use  $y = 0.1$ , which should be considered as an upper limit on the helium abundance.

Only models strongly depleted in carbon match the carbon lines, while all nitrogen lines in the optical suggest an enrichment in nitrogen. As for HD 16691,  $N\ \text{IV}\ \lambda 4054$  appears as a strong emission in our models, which we could not reconcile with the observed profile (a very weak emission). The  $O\ \text{III}\ \lambda 5592$  line shows that oxygen is also depleted. Qualitatively, the CNO abundances are consistent with the evolved nature of HD 15570, as inferred from its position in the H-R diagram.

The best agreement for wind-sensitive lines was obtained with clumped models, still requiring a sub-solar phosphorus abundance to match  $P\ \text{V}\ \lambda 1118-1128$  (see Table 4).

#### 5.5. HD 14947 - O5 If

The best fit was obtained for  $T_{\text{eff}} = 37000 \pm 1000\ \text{K}$ , which is 1500 K cooler than expected from the  $T_{\text{eff}}$  - spectral type calibration by Martins et al. (2005). This  $T_{\text{eff}}$  is low enough that the  $C\ \text{III}\ \lambda 5696$  line is present in the spectrum and can be used to measure the carbon abundance, which is mildly depleted. The adopted value also gives a consistent fit to  $C\ \text{III}\ \lambda 4647-50-52$  and  $C\ \text{IV}\ \lambda 5801-5812$ . We obtained a consistent fit to several nitrogen lines, including  $N\ \text{III}\ \lambda 4634-4640-42$ ,  $N\ \text{III}\ \lambda 4510-4515$ ,  $N\ \text{IV}\ \lambda 5204-5205$  and  $N\ \text{IV}\ \lambda 6380$  by adopting a surface enrichment comparable to those we measured in other stars of this sample. Similarly,  $O\ \text{III}\ \text{FUV triplet} (\lambda 1150-1154)$  and  $O\ \text{III}\ \lambda 5592$  indicate a depletion in oxygen. Qualitatively, the CNO patterns are compatible with both the evolutionary status (indicated by the position of HD 14947 in the H-R diagram), and the relatively minor He enhancement ( $y = 0.12$ ).

The UV and optical wind lines could only be fitted with very highly clumped models. The best fit was obtained for a model with  $f_{\infty} = 0.03$ , implying a reduction of a factor of six for the mass-loss rate compared to the homogeneous model. This is by far the highest reduction of the whole sample. This highly clumped model is dictated by the  $P\ \text{V}$  resonance doublet, for which we could achieve a very good fit by adopting a normal solar abundance for phosphorus. Using this low filling factor also maintains a good fit to all other wind/clumping-sensitive lines (see Sect. 4). At the temperature we derive for HD 14947, the effect of introducing clumping is to strongly recombine  $P^{+4}$  ion to  $P^{+3}$  and the former ion is no longer dominant. The opacity in the line is greatly reduced and thus there is no additional need to vary the abundance to improve the fit.

#### 5.6. $\lambda\ \text{Cep}$ - O6 I(n)fp

This star is another famous rapid rotator, with conspicuous spectral variability (e.g. Howarth & Prinja 1996; Kaper et al. 1997).

The best fit we could achieve to the FUV/UV and optical spectra was for  $T_{\text{eff}} = 36,000$  K,  $\log g = 3.5$ . Despite the high rotation rate, several lines are available for accurate abundance determinations. We found that  $\lambda$  Cep is only moderately enriched in nitrogen, and depleted in carbon and oxygen (Table 4), which is quite surprising because more extreme patterns would be expected from rotational mixing in such a fast rotator. We also found that  $y = 0.12$ , in line with this moderate chemical evolution.

The introduction of clumping in the model dramatically improved the fit to the spectrum, including H $\alpha$ . Here again, we needed a lower-than-solar phosphorus abundance to achieve the fit to the P v FUV lines presented in Fig. A.12. As discussed in Sect. 6.4, this indicates that the model optical depth for the resonance doublet is too high for solar abundance, which likely implies that either the ionization balance of phosphorus is computed incorrectly by CMFGEN, or that its treatment of clumping is incomplete.

The most severe disagreement between the model and the observations is for He II  $\lambda 4686$  – with or without clumps we fail to reproduce the double-peaked profile, which is typical of a high rotation rate. In this context it is no surprise that the N III  $\lambda\lambda 4634$ -4640-4642 lines present the same profile as already observed in  $\zeta$  Puppis and HD 16691.

### 5.7. HD 163758 - O6.5 Iaf

A low effective temperature  $T_{\text{eff}} = 32,500 - 33,000$  K would provide a very good fit to the forest of photospheric iron ions lines in the FUV-UV domain (see also Bianchi & Garcia 2002). However, such a cool effective temperature is ruled out from the analysis of the optical spectrum and  $T_{\text{eff}} = 34,500 \pm 1000$  K is preferred to fit the He I and He II lines in the optical and the FUV-UV spectrum as well. Although significantly higher than the UV-based  $T_{\text{eff}}$ , it is also more compatible with the spectral type of the star (Martins et al. 2005). We found no documented variability that would explain the contradictory conclusions reached from the *FUSE* - *IUE* spectra on one hand and optical spectra on the other hand.

The carbon lines in HD 163758 are stronger than in other O supergiants of similar spectral type (Gómez & Niemela 1987a). This is the case for lines in emission (e.g. C III  $\lambda 1247$ , C III  $\lambda\lambda 4647$ -50-52 and C III  $\lambda 5696$ ) or in absorption (e.g. C III  $\lambda 4068$  or C IV  $\lambda\lambda 5801$ -5812). All these suggest that this star is carbon-rich. Our analysis shows that HD 163758 is indeed the most carbon-rich star of our sample, with an abundance of one and a half times the solar carbon abundance. While this abundance allows model spectra to match most photospheric C III and C IV lines, it still does not reproduce the strong C III  $\lambda 5696$  emission line.

HD 163758 is also one of the most nitrogen-rich stars of the sample, as indicated by the strong emission lines of N III  $\lambda\lambda 4634$ -4640-4642 (the N III  $\lambda\lambda 1748$ , 1752 absorption lines are saturated). Because nitrogen is produced at the expense of carbon, and assuming mixing processes are unchanged when super-solar element abundance are present, this suggests that the initial carbon abundance of this object was very high. On the other hand, the oxygen abundance is sub-solar, as indicated by the very good fits to the photospheric O III lines in the FUV ( $\lambda\lambda 1150$ , 54) and optical ( $\lambda 5592$ ) spectrum. This seems at odds with the conclusion that the initial CNO mixture of this star was super-solar.

Whatever parameters we chose to fit the photospheric features, the whole set of wind lines could only be matched with a clumped models. The improvement is especially striking for the

Si IV  $\lambda\lambda 1394$ -1403 resonance doublet; this suggests that for this range of effective temperature, Si IV in addition to P v, can be used to probe clumping, thus extending the conclusions reached by Prinja & Massa (2010) for B-type supergiants up to significantly higher temperatures (or different ionization fractions).

### 5.8. HD 192639 - O7.5 Iabf

The best fit was obtained for  $T_{\text{eff}} = 33,500 \pm 1000$  K. In contrast to HD 163758, the analysis of both FUV-UV and optical spectra yields consistent results for HD 192639. Given the strong line variability of this star, especially in the He II  $\lambda 4686$  line (e.g. Rauw et al. 2001), and the long time span separating the FUV, UV and optical spectra, this is quite remarkable.

Our analysis indicates that HD 192639 is moderately depleted in carbon and oxygen, although its nitrogen enrichment is relatively stronger. Whatever carbon abundance we used, we could not reproduce the C III  $\lambda 5696$  or C IV  $\lambda\lambda 5801$ -5812 lines with the correct intensity (see Fig. A.16). Note that the latter would be better reproduced using higher  $T_{\text{eff}}$ , which is ruled out from the fit of He lines. The carbon abundance we quote is the upper limit above which C III  $\lambda 4068$  and C III  $\lambda\lambda 4647$ -50-52 become stronger than observed. The nitrogen abundance is constrained from the strong N III lines in the optical at  $\lambda\lambda 4510$ -4515 and N III  $\lambda\lambda 4634$ -4640-42. The N III  $\lambda\lambda 1748$ -1752 lines are saturated and were not used. This abundance is consistent with other N III diagnostics, including N III  $\lambda 5320$ -5327 in emission, but fail to reproduce the weak absorption of N IV  $\lambda\lambda 5204$ -5205. Oxygen lines are altogether very well defined and responsive to variations of abundances, either in the UV or in the optical.

Finally, clumped models are needed to reproduce the wind lines, together with a factor of two depletion of the phosphorus abundance, compared to solar, to fit the P v FUV lines. As for HD 163758, the improvement in the fit resulting from clumped models is striking for the Si IV  $\lambda\lambda 1394$ -1403 doublet.

## 6. Discussion

### 6.1. Evolutionary status

We constructed the H-R diagram of the sample using effective temperatures and luminosities derived from the modeling, as well as evolutionary tracks and isochrones from Meynet & Maeder (2003) (see Fig. 3), with an initial rotational velocity of  $300 \text{ km s}^{-1}$  and solar metallicity. The most remarkable feature of this diagram is how well it distinguishes the different spectral types in terms of masses and ages. The O4 supergiants cluster tightly around the  $60 M_{\odot}$  track, 3 Myr isochrone. Later spectral types probe lower masses or more evolved regions of this diagram, but in any case, the stars are more massive than  $40 M_{\odot}$  and younger than 5 Myr.

Alternately, the position of the O4 supergiants in this diagram might be explained by assuming that they are in fact much older, and located on the  $60 M_{\odot}$  track in the range 4.3 Myr to 4.4 Myr. However, the predicted properties of this track in this age range, like the hydrogen mass fraction for instance, are incompatible with the observed properties of the O4 supergiants. Indeed, we find  $X(\text{H}) = 55\%$  or higher while  $X(\text{H}) \approx 4\%$  or lower should be expected for a star with initial mass  $60 M_{\odot}$  after 4.3 Myr. This definitively rules out this possibility. For the same reason, the O4 stars of this sample could not be stars with initial masses slightly above  $85 M_{\odot}$ , which would be around 3.7 Myr old, because the expected  $X(\text{H})$  is 5% or less. The same comment holds for the later-type stars though for different initial masses.

**Table 3.** Fundamental parameters and wind properties for the stars in our sample.

Star HD	$T_{\text{eff}}$ [kK]	$\log g_c$	$\log \frac{L}{L_{\odot}}$	$\log(M)$	$v_{\infty}$ [km s <sup>-1</sup> ]	$\beta$	$f_{\infty}$	$v_{\text{cl}}$ [km s <sup>-1</sup> ]	$v \sin i$ [km s <sup>-1</sup> ]	$v_{\text{mac}}$ [km s <sup>-1</sup> ]	$M_{\text{spec}}$ [ $M_{\odot}$ ]	$M_{\text{evol}}^t$ [ $M_{\odot}$ ]	$M_{\text{evol}}^{\text{init}}$ [ $M_{\odot}$ ]	Age [Myr]
16691	41.0	3.66	5.94	-5.52	2300	1.2	0.06	130	135	37	56.6 <sup>+14.6</sup> <sub>-11.7</sub>	53.4	65.2 <sup>+9.5</sup> <sub>-8.6</sub>	3.1 <sup>+0.5</sup> <sub>-0.1</sub>
66811	40.0	3.64	5.91	-5.70	2300	0.9	0.05	100	210	90	56.1 <sup>+14.5</sup> <sub>-11.6</sub>	51.1	62.3 <sup>+8.1</sup> <sub>-7.8</sub>	3.2 <sup>+0.4</sup> <sub>-0.2</sub>
190429A	39.0	3.62	5.96	-5.68	2300	1.0	0.04	30	150	57	66.0 <sup>+17.4</sup> <sub>-13.4</sub>	54.6	68.0 <sup>+8.3</sup> <sub>-6.3</sub>	3.3 <sup>+0.4</sup> <sub>-0.2</sub>
15570	38.0	3.51	5.94	-5.66	2200	1.1	0.05	30	97	40	54.0 <sup>+14.0</sup> <sub>-11.1</sub>	48.7	59.5 <sup>+6.6</sup> <sub>-6.7</sub>	3.4 <sup>+0.8</sup> <sub>-0.1</sub>
14947	37.0	3.52	5.83	-5.85	2300	1.3	0.03	30	130	36	48.0 <sup>+12.4</sup> <sub>-9.8</sub>	43.4	51.2 <sup>+6.0</sup> <sub>-5.1</sub>	3.9 <sup>+0.5</sup> <sub>-0.5</sub>
210839	36.0	3.54	5.80	-5.85	2100	1.0	0.05	120	210	80	51.4 <sup>+15.2</sup> <sub>-12.0</sub>	42.3	50.5 <sup>+4.4</sup> <sub>-4.5</sub>	4.0 <sup>+0.2</sup> <sub>-0.2</sub>
163758	34.5	3.41	5.76	-5.80	2100	1.1	0.05	30	94	34	41.6 <sup>+10.8</sup> <sub>-8.5</sub>	41.2	48.0 <sup>+3.0</sup> <sub>-4.2</sub>	4.1 <sup>+0.3</sup> <sub>-0.3</sub>
192639	33.5	3.42	5.68	-5.92	1900	1.3	0.05	30	90	43	38.3 <sup>+9.4</sup> <sub>-8.2</sub>	39.1	43.0 <sup>+4.6</sup> <sub>-3.7</sub>	4.2 <sup>+0.3</sup> <sub>-0.2</sub>

$M_{\text{spec}}$ ,  $M_{\text{evol}}^{\text{init}}$ ,  $M_{\text{evol}}^t$  refer to spectroscopic mass, initial mass and mass at the corresponding stellar age, respectively. Uncertainties for  $T_{\text{eff}}$  are  $\pm 1000$  K,  $\pm 0.1$  dex for  $\log g$  and  $\pm 0.1$  dex on  $\log L/L_{\odot}$  (reflecting the uncertainty on the distance). An uncertainty of  $\pm 0.2 \times 10^{-6} M_{\odot} \text{ yr}^{-1}$  was estimated for the mass-loss rates.  $v_{\infty}$  is measured within  $\pm 100$  km s<sup>-1</sup>.

**Table 4.** He, C, N, O and P abundances.

Star	y(He/H)	$\epsilon(\text{C})$	$\epsilon(\text{N})$	$\epsilon(\text{O})$	$\epsilon(\text{P})$	$\epsilon(\Sigma \text{CNO})$	X(C)	X(N)	X(O)
HD 16691	0.15	6.52 $\pm$ 0.18	9.00 $\pm$ 0.17	7.83 $\pm$ 0.25	5.05 $\pm$ 0.24	9.03	1.00E-04	8.63E-03	6.67E-04
HD 66811	0.16	7.60 $\pm$ 0.25	9.10 $\pm$ 0.17	8.13 $\pm$ 0.30	5.05 $\pm$ 0.26	9.16	2.86E-04	1.05E-02	1.30E-03
HD 190429A	0.15	7.09 $\pm$ 0.18	8.92 $\pm$ 0.16	7.83 $\pm$ 0.26	5.26 $\pm$ 0.20	8.96	9.10E-05	7.27E-03	6.69E-04
HD 15570	0.10	7.52 $\pm$ 0.16	8.62 $\pm$ 0.15	8.30 $\pm$ 0.24	5.06 $\pm$ 0.18	8.81	3.27E-04	4.79E-03	2.63E-03
HD 14947	0.12	8.30 $\pm$ 0.16	8.78 $\pm$ 0.12	8.13 $\pm$ 0.24	5.25 $\pm$ 0.15	8.97	1.66E-03	5.00E-03	1.44E-03
HD 210839	0.12	8.22 $\pm$ 0.21	8.70 $\pm$ 0.15	8.48 $\pm$ 0.14	4.70 $\pm$ 0.18	8.99	1.32E-03	4.67E-03	3.23E-03
HD 163758	0.15	8.56 $\pm$ 0.16	8.78 $\pm$ 0.16	8.36 $\pm$ 0.19	5.02 $\pm$ 0.21	9.08	2.72E-03	5.19E-03	2.25E-03
HD 192639	0.15	8.17 $\pm$ 0.17	8.76 $\pm$ 0.15	8.61 $\pm$ 0.21	5.07 $\pm$ 0.17	9.05	1.09E-03	5.01E-03	4.01E-03
Ori OB1 (B stars)	...	8.35 $\pm$ 0.03	7.82 $\pm$ 0.07	8.77 $\pm$ 0.03	...	8.92	1.96E-03	6.77E-04	6.43E-03
Sun 3D	0.09	8.39 $\pm$ 0.05	7.78 $\pm$ 0.05	8.66 $\pm$ 0.05	5.36 $\pm$ 0.03	8.88	2.16E-03	6.18E-04	5.35E-03

By convention  $\log \epsilon(X) = 12 + \log [X/H]$ . For comparison, we give the solar chemical composition determined by Asplund et al. (2005, Sun 3D) and the chemical composition of B stars of the Ori OB1 association determined by Simón-Díaz (2010) and Nieva & Simón-Díaz (2011). Mass-fractions are also indicated for CNO.

The luminosities were derived for the sample stars under the assumption that they are single. If they turn out to be binaries, the luminosity of each component would have to drop, thus translating into lower initial masses and a somewhat different ages for the stars. As already stated (Sect. 2.1), seven of the eight stars in our sample are most likely single and the known binary is well separated, therefore we were able to use photometry of the primary for the luminosity calculation.

When studying the most massive stars in the Arches cluster, Martins et al. (2008) found a significant overlap between the positions of the faintest WN7-9h stars and the most luminous, “extreme”, O supergiants in their sample, which turned out to have spectral types O4-6I<sup>+</sup>. The positions of the stars of our sample in the H-R diagram overlap with the stars studied by Martins et al. (2008) of the same spectral class. We note that HD 190429A and HD 16691 show a late-type WN spectrum in the infrared *K* band (Conti et al. 1995) and could be regarded as “transitional” objects in terms of evolutionary properties, much like the extreme OI<sup>+</sup> found by Martins et al. (2008), although they are systematically less luminous. When merged with those from Martins et al. (2008), our results confirm that the position of WN7-9h stars and O supergiants is distinct in the H-R diagram.

Another insight into the evolutionary status of the stars is shown in Fig. 4, where the hydrogen mass fraction is plotted against the stellar luminosity. It is clear from Fig. 4 that all stars in our sample are on the early part of their evolution away from the zero-age main-sequence, even the most extreme of them

(HD 190429A). Compared to the results from Martins et al. (2008) our stars appear to be more evolved (more hydrogen-depleted or equivalently helium-enriched) than their sample of supergiants, either normal or extreme. The reason for this difference is unclear, because helium lines in the near-infrared are as sensitive to variations of helium content as lines in the optical range. A younger age of these cluster stars and possibly a higher metallicity could influence both their evolution and spectra.

## 6.2. Masses

The spectroscopic masses were derived after correcting the effective gravity derived from the analysis by the effect of centrifugal forces caused by rotation (see Table 3), following the approach outlined in Repolust et al. (2004). Assuming a random distribution of orientations for the rotational axis, the true surface gravity  $g_c$  is the sum of the effective gravity  $g_{\text{eff}}$  and a correction term. To a good approximation, the centrifugal acceleration averaged over the stellar disk is given by the projected rotational velocity, whence  $g_c = g_{\text{eff}} + (v \sin i)^2/R_*$ . For the stars in our study, the corrections are small, with  $\Delta \log g \leq 0.04$ , which corresponds to a correction lower than 10% for the actual mass.

Evolutionary masses are obtained by bilinear interpolation between the tracks and isochrones in the H-R diagram. In Table 3, we list masses at the corresponding stellar age and the original mass. Spectroscopic masses and evolutionary masses (at the star age) generally agree well. The difference is below 10% for

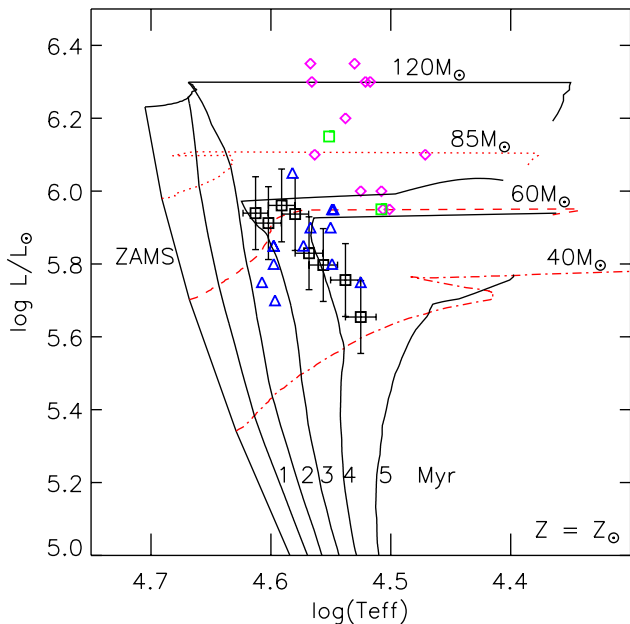


**Fig. 3.** H-R diagram showing the program stars (black squares) and the stars from Martins et al. (2008) for comparison. Blue triangles are “normal” O4-6 supergiants, green squares are “extreme” O4-6I<sup>+</sup> stars, pink diamonds are WN7-9h objects. Evolutionary tracks and isochrones are from Meynet & Maeder (2003) with an initial rotation of  $300 \text{ km s}^{-1}$ .

HD 16691,  $\zeta$  Puppis, HD 190429A, HD 14947, HD 163758, and HD 192639, while it is around 20% for HD 15570 and  $\lambda$  Cep. For the most part, the observed differences could result from uncertainties in  $\log g$ . Assuming the stellar distance is known, the error in  $\log g$  is the dominant source of error in the spectroscopic mass, hence in the ratio of the evolutionary mass to the spectroscopic mass. These uncertainties are partially attributable to the difficulties associated with rectifying echelle spectra, especially in the vicinity of broad H lines. If accurate surface gravities are to be obtained, it is crucial that observing procedures are adopted to facilitate rectification, and to allow the accuracy of the rectification to be verified (e.g., measurement of multiple standards). Ideally, it would be useful to check the rectification against lower resolution (but still high-signal-to-noise) spectra. Obviously, distance determinations to Galactic O stars are quite uncertain (at least for field stars) and we cannot discard just yet the contribution of distance uncertainties as an important potential source of errors in spectroscopic masses.

Likewise, continued progress in stellar evolution theory confirms that stellar rotation is another fundamental physical process that affects the evolution of massive stars. The global agreement reached with spectroscopic masses furthermore suggests that, along with the introduction of NLTE line-blanketed stellar atmospheres, the assumptions adopted in the evolution models provide a realistic description of the actual conditions in young early-type massive objects.

$\zeta$  Puppis is very interesting in this context. It is likely seen near equator-on (Harries 2000, and refs. therein), which implies that its true rotation rate should be  $210 \text{ km s}^{-1}$  or slightly higher. Applying the centrifugal correction to the measured surface gravity, we derive an actual (spectroscopic) mass of  $56 M_{\odot}$ , while the initial mass, as derived from the star’s location in the H-R diagram is  $62 M_{\odot}$  (cf. Table 3). The evolutionary model

with an initial mass of  $60 M_{\odot}$  and an initial rotation rate of  $v \sin i = 300 \text{ km s}^{-1}$  that best represents the position of  $\zeta$  Puppis shows that after 3.2 Myr, the stellar mass should be  $\approx 50 M_{\odot}$  and the rotation rate  $\approx 108 \text{ km s}^{-1}$ , more than  $100 \text{ km s}^{-1}$  lower than the measured equatorial velocity of the star. Either the initial rotation velocity of  $\zeta$  Puppis was higher than  $300 \text{ km s}^{-1}$  or the star has been spun up during its evolution. Estimating the real value for the initial rotation rate is not possible because too many other quantities are involved in the evolution of the star’s angular momentum. For instance the mass-loss rates, as measured from this study, are a factor two to three times lower than the values from Vink et al. (2000), which were adopted in the evolution models of Meynet & Maeder (2003). After 3.2 Myr a  $60 M_{\odot}$  (initial mass) star should have lost only  $3 M_{\odot}$  rather than  $8 M_{\odot}$  (assuming the other parameters would still evolve according to the higher mass-loss scenario).

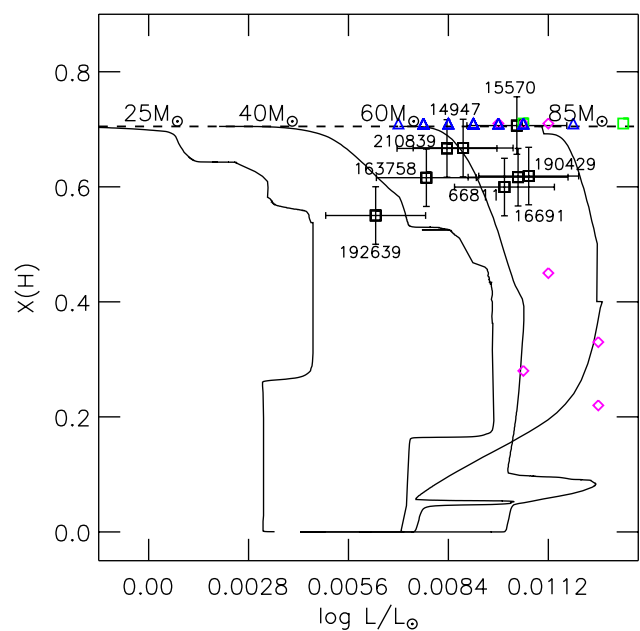


**Fig. 4.** Hydrogen mass-fraction as a function of luminosity. Symbols are the same as in Fig 3. Full lines are for Geneva models with an initial rotational velocity of  $300 \text{ km s}^{-1}$  (Meynet & Maeder 2003). The dashed line indicates the initial value  $X(\text{H})=0.705$

### 6.3. Surface abundances

#### 6.3.1. Helium and nitrogen

To assess the chemical evolutionary status of the stars in our sample, we compared the nitrogen to helium mass-fraction ratio as a function of effective temperature to predictions from stellar evolution models. According to stellar evolution, nitrogen and helium are produced during the hydrogen burning phase but the relative increase of abundances is larger for nitrogen than for helium, since the latter is already abundant in the atmosphere while the former is not. The N/He ratio quickly evolves from the initial value to a value corresponding to the CNO equilibrium, and stars for which the equilibrium has not been reached will present intermediate values of N/He.

Two of the O4 supergiants, HD 16691 and  $\zeta$  Puppis, seem slightly offset in this diagram, and masses higher than inferred



from the H-R diagram would be needed to account for their position. In both cases, this is a consequence of the strong nitrogen enrichment we derive rather than from too small a helium mass-fraction, which we find to be normal for this range of masses and ages. The case of HD 15570 is the exact opposite: a moderate nitrogen enrichment and low helium abundance shifts the star up in the diagram. Although HD 190429A is a binary, its properties seem well described by standard evolution models. The location of these two stars in Fig. 5 also indicates that they will soon reach the CNO equilibrium (possibly the case for HD 14947 as well).

Similarly, the location of the later-type stars (cooler  $T_{\text{eff}}$ ) in this diagram is consistent, both qualitatively and quantitatively, with the predicted N/He fraction from stellar evolution models for objects in the mass range  $50 - 40 M_{\odot}$ . These stars lie in a region of the plot where the N/He ratio is still rising, which indicates that the CNO equilibrium has not been attained.

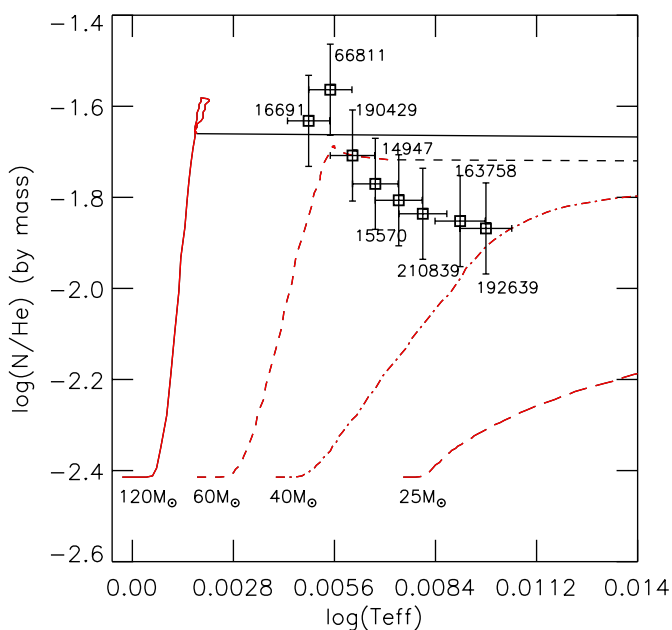


**Fig. 5.** Ratio of nitrogen-to-helium mass-fraction as a function of effective temperature, as predicted in Geneva models for stars with an initial rotation rate of  $300 \text{ km s}^{-1}$  (Meynet & Maeder 2003), and as derived from this study (symbols). The red part of each line corresponds to the part of evolutionary tracks where  $X(\text{H}) \geq 0.4$ .

### 6.3.2. Carbon versus nitrogen

Together with the surface enrichment of nitrogen, the stars in our sample reveal carbon depletion, resulting in significant increases of the N/C ratios. This ratio is an excellent tracer of the chemical evolution of massive stars, because it increases substantially when CNO cycle-processed material appears at the stellar surface.

Figure 6 presents a comparison between the measured N/C ratios (mass-fractions) and the predictions of the Geneva stellar evolution models, as a function of stellar age. We can use this plot, together with the H-R diagram, to check whether a star is evolving according to the prediction of standard evolutionary tracks. We find two different behaviors – one for O4-type supergiants and the other for later-type (O5 to O7.5) supergiants. The measured N/C ratio of this later group behaves qualitatively and

quantitatively as predicted by stellar evolution models. These stars are less massive and older (around 4 Myr or older) than the first group of objects between 3 and 3.5 Myr. In the early-type, younger, group, N/C ratios are higher than predicted for the corresponding masses. For HD 16691 and HD 190429A, it is about ten times higher than predicted by any evolutionary model, which additionally confirms the advanced evolutionary status of these objects.

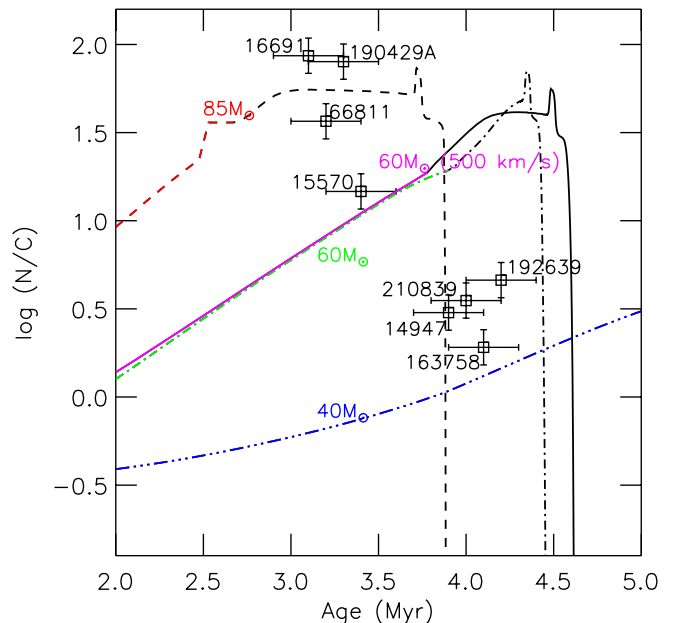


**Fig. 6.** Evolution of the ratio of nitrogen-to-carbon mass-fractions as a function of time in Geneva models (Meynet & Maeder 2003). The full (black) line is for a model with  $60 M_{\odot}$  and an initial rotation velocity of  $500 \text{ km s}^{-1}$ . Overplotted in red, green, blue and pink are the parts of the tracks corresponding to the main-sequence phase (more exactly the part of the hydrogen burning phase where  $X(\text{H}) \geq 0.4$ ).

Maeder et al. (2009) recently highlighted that N/C ratios depend on many variables including stellar age, mass, metallicity, rotational velocity, and multiplicity or magnetic fields and warned against an overinterpretation of measurements compared to theoretical predictions. However, taken at face value, these plots suggest that the global efficiency of mixing in stars more massive than  $60 M_{\odot}$  is underestimated in stellar evolution models for a given rotation rate.

In Fig. 6 we also show the expected N/C ratio as a function of age for a  $60 M_{\odot}$  model with an initial rotation velocity of  $500 \text{ km s}^{-1}$ . The primary effect of increasing the initial rotation velocity is to maintain the N/C ratio at its maximum value up to 4.6 Myr (shift by 0.15 Myr compared to a model with  $300 \text{ km s}^{-1}$ ). This rotation increase has no effect in the region of the plot where the O4 supergiants are located, i.e. around 3 Myr. Hence, a spread in rotation rates appears unable to account for the higher N/C ratios we observe.

Two stars of our sample, HD 66811 and HD 210839, have high rotation rates with  $v \sin i \geq 210 \text{ km s}^{-1}$ . HD 16691 has a lower  $v \sin i$  ( $\approx 135 \text{ km s}^{-1}$ ) but presents several spectral characteristics usually associated with a high rotation rate (N III and C III, He II  $\lambda 4686$ , H $\alpha$ , see Sect. 5.3 and Appendix A). HD 66811 and HD 16691 have the strongest nitrogen enrichment of the

sample and HD 16691 the lowest carbon abundance (hence the highest N/C ratio). Both stars support the idea that rotational mixing is responsible for the surface composition changes. On the other hand, HD 210839, which also has a high rotation rate, goes against this conclusion because it has the lowest nitrogen enrichment and marginal carbon depletion. The other stars have intermediate  $v \sin i$  and no correlation emerges with the N/C ratio. This contradictory result is reminiscent of the findings of Hunter et al. (2007), though we stress that our sample is too small for a statistical interpretation.

Let us now compare how the carbon and nitrogen mass-fractions relate to each other in a diagram where  $X(C)$  is plotted as a function of  $X(N)$ . It is expected that in the early phases of stellar evolution,  $X(C)$  decreases, while  $X(N)$  is built up at the expense of carbon. Fig. 7 shows that, as expected, stars with higher nitrogen content show stronger carbon depletion. For the measured stellar masses, and for stars still evolving in the hydrogen burning phase, the observed range of the nitrogen mass-fractions is qualitatively compatible with the predictions of stellar evolution models. However, quantitative differences are observed. Six out of eight stars cluster in a region where the carbon depletion is too strong for the measured nitrogen enrichment (or alternatively, nitrogen enrichment is too low for the measured carbon depletion). Once again, we observe a dichotomy in the behavior of the O4 supergiants and the O5 - O7.5 supergiants. The former group of stars, with masses  $\approx 60 M_{\odot}$ , shows the strongest carbon depletion, which is so extreme in two cases that it would not be reached in any model at any evolutionary phase. In this context it is interesting that these stars show WN spectral features in their near-infrared spectra (Conti et al. 1995). Only HD 14947 (and HD 163758 to a lesser extent, given its very peculiar abundances) agree qualitatively and quantitatively with the 40 - 60  $M_{\odot}$  models that are expected to best describe the properties of this sample. This agreement probably means that both stars are actually very close to CNO equilibrium. Furthermore, the position of HD 163758 in Fig. 7 is consistent with its carbon-rich status as quoted from observations by Gómez & Niemela (1987b).

### 6.3.3. CNO

In massive stars, the total mass fraction of CNO remains roughly constant during the CNO cycles. In the early phases of evolution, the CN-equilibrium is achieved first while the oxygen content remains about constant, and somewhat later enters the burning cycle. The full CNO-equilibrium is achieved only after a significant amount of hydrogen has been burnt in the core. Changes in the oxygen surface abundance are only expected in later stages in the more massive and faster rotating models.

In Fig. 8, we compare our N/C versus N/O ratios to those predicted by stellar evolution models for different masses and  $X(H) \geq 0.4$  (Meynet & Maeder 2003). This plot indicates whether the variations of N/C and N/O follow the trend expected for material processed through the CNO cycle. The amplitudes of the departure from the initial abundance ratios are notoriously sensitive to differences in rotational velocities, masses, and ages.

For the O4 supergiants, N/C ratios are too high for the measured N/O ratios, compared to predictions by the evolution models. For three stars, their location in Fig. 8 indicates that their N/C and N/O ratios are consistent with more advanced evolutionary status (WNs) than actually derived. The fourth star, HD 15570, exhibits different properties: although its N/C and N/O ratios are slightly higher than those predicted by evolutionary models for 60  $M_{\odot}$ , they are nevertheless compatible with its evolution-

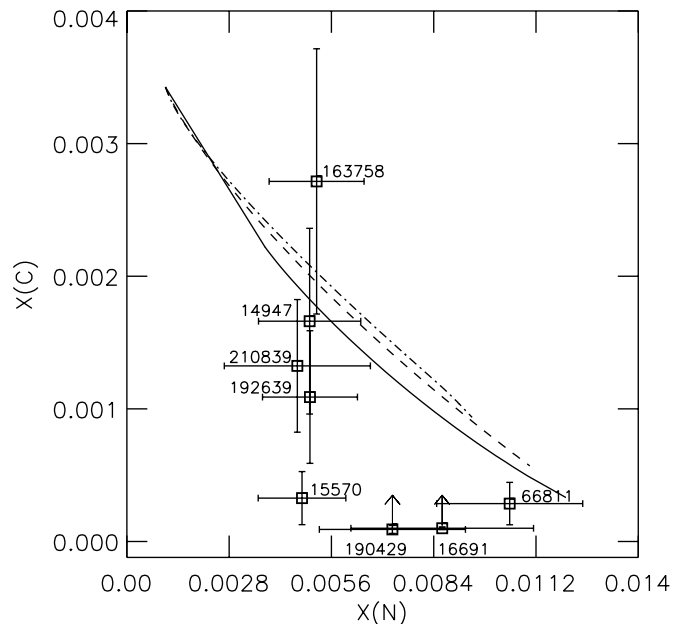


**Fig. 7.** Carbon mass-fraction as function of nitrogen mass-fraction, as predicted by Geneva models with an initial rotation velocity of 300  $\text{km s}^{-1}$  (Meynet & Maeder 2003). Solid line is for 85  $M_{\odot}$ , dashed for 60  $M_{\odot}$ , and dot-dashed for 40  $M_{\odot}$ . Symbols are for values derived from this study.

ary status. Within this group of stars, the observed behavior is qualitatively compatible with the expected evolution: the more massive stars are farther along the evolutionary tracks than the less massive ones, assuming that they are in the same evolutionary phase/status (as suggested by the H-R diagram, cf. Fig. 3).

The opposite behavior is observed for later- and mid-type supergiants, whose measured N/C ratios are lower than predicted from evolution models for stars in the 40 - 60  $M_{\odot}$  range (for the measured N/O ratios).

The case of HD 163758 is noteworthy because it presents unusual abundance patterns (see Sect. 5.7), including a super-solar carbon abundance and a very high nitrogen content while being only mildly oxygen-depleted. Such patterns likely result from a non-standard (non solar-like) original mixture of CNO elements, and the relative enhancement of the nitrogen mass-fraction depends on the initial carbon abundance available for conversion during the CNO-cycle.

Figure 7 indicates that the nitrogen enrichment in HD 14947 is consistent with the carbon depletion predicted for a 50  $M_{\odot}$  star. Moreover, Fig. 6 indicates that the measured N/C ratio is consistent with the age of the star. From these two results, we conclude that the measured N/C ratio is compatible with the predictions of stellar evolution models. Therefore, the position of HD 14947 in Figure 8 suggests that N/O is too high compared to evolutionary predictions, or in other words, that the measured oxygen abundance is too low (lower than predicted). If the oxygen depletion is not the result of abnormal initial abundances, it could be explained if deeper layers of the star are exposed to the surface, for example by deeper mixing than predicted by the rotating models. Alternatively it could be explained by stripping of the star by winds or a binary companion; or by the accretion of oxygen-depleted layers from a former companion (Langer et al. 2008; de Mink et al. 2011).



We note that the total of the CNO abundances of the sample stars (see Table 4) shows that with a mean combined abundance  $\epsilon(\Sigma\text{CNO}) = 9.02$ , the initial CNO mixture for several objects is potentially different from the assumed standard cosmic abundances adopted for the computation of the stellar evolution models by Meynet & Maeder (2003). Because there is evidence for a significant spread in the metallicity for solar-type stars in the thin disk ( $\sigma[\text{Fe}/\text{H}] = 0.191$  dex, Fuhrmann 2011), there might be a spread in the actual Fe abundances in O-type stars as well. Although solar values were assumed in our study, they might not be relevant for all our sample stars.

Although striking, the scatter in N/C and N/O ratios for this sample is real, as indicated by their very similar spectra (hence physical parameters) but different CNO line intensities. For the first group of stars (HD 16691, HD 190429A, HD 66811, HD 15570), the amplitude of the deviation from the models is low enough that differences in the initial abundances could help reconcile the outputs from stellar evolution models and our measurements. The slope of the theoretical tracks is very sensitive to the adopted initial mixture (see, e.g., Fig. 3 of Przybilla et al. 2010) and a span of N/O and N/C ratios is expected. Including magnetic fields in stellar evolution models could also change the speed and amplitude at which abundance patterns are built up at the surface. A recent study by Meynet et al. (2011) confirmed that the inclusion of magnetic braking yields very different results for the surface abundances, which depend on the assumed rotation law inside the star. For stars with differential rotation, mixing is faster and stronger, but for stars with solid-body rotation, mixing is inhibited because the stars spin down rapidly. In this case, surface abundance ratios are lower than in models without magnetic braking. However, Meynet et al. (2011) obtained results for a  $10 M_{\odot}$  star and dedicated simulations would be necessary to confirm that more massive stars with magnetic fields can still be rotating relatively normally and produce significant changes in surface abundance ratios after a few Myr.

For the second group of (later) stars, an obvious solution appeals to models with higher rotation velocities, which exhibit more mixing. Again, if magnetic braking plays a role, mixing would be modified (see above). Alternatively, (close) binarity would affect the evolution and likely the surface abundances of the stars (from mixing and possibly mass transfer). Binarity would also imply different luminosities, hence evolutionary masses. In any case, comparison with tailored models for magnetic braking (and/or lower masses) would be required for more quantitative conclusions.

The interplay between rotational mixing and mass-loss as currently implemented in the models might not be efficient enough to account for the observed the CNO patterns. We note in this context that we derive mass-loss rates up to three times lower than those used in the calculations of evolution models (see Sect. 6.4). The actual metal content in the Geneva evolutionary models is also higher than what is measured in the solar neighborhood (0.02 versus 0.014) by Przybilla et al. (2008) (2008), which best corresponds to the global metallicity of the stars of the present sample. Both these facts undermine the direct comparison of our measurements with chemical patterns from stellar evolution models for an assumed  $Z/Z_{\odot} = 0.02$ .

The overall properties of these objects, including their location in the H-R diagram and hydrogen mass-fraction (see Fig. 3 and Fig. 4), indicate that they are observed at different stages of their chemical evolution, even though they are of very similar age. The underlying drivers of the observed differences are unclear and could be manifold – from enhanced mixing related to binary evolution in an earlier phase prior to the supergiant stage

to evolution with rotation and a magnetic field (Meynet et al. 2011). Recent results by Sana & Evans (2011) suggest that the binary fraction among massive stars is at least as high as 50%. Although all but one star in the present sample are believed to be single, we cannot exclude the possibility that some of them might have been members of a binary system in the past; this scenario is especially appealing for runaway stars like  $\zeta$  Puppis (or HD 16691). On the other hand, the observed properties of the only massive binary in our sample, HD 190429A, are qualitatively similar to those of the other stars of the same spectral type, and no clear influence of the secondary in this system is found. Nevertheless, since binarity is expected to have significant consequences for stellar evolution, tailored evolutionary models would be needed to compare to our measurements and to draw firmer conclusions.

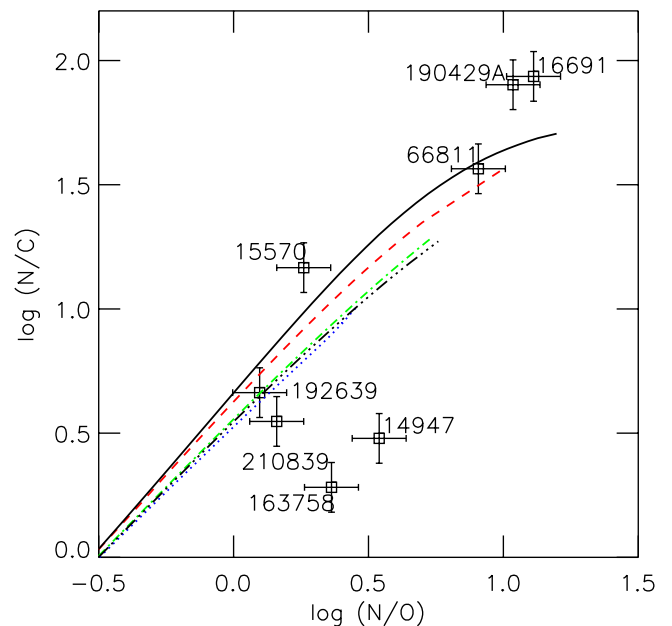


**Fig. 8.** N/O vs. N/C abundance ratio (by mass) measured for the sample stars and compared to the ratios predicted in Geneva models (Meynet & Maeder 2003). Solid line is for  $120 M_{\odot}$ , dashed red line is for  $85 M_{\odot}$ , dot-dashed green line is for  $60 M_{\odot}$ , and dotted blue line is for  $40 M_{\odot}$ . The black dot-dot-dot-dashed line is for a model with  $60 M_{\odot}$  and  $v \sin i = 500 \text{ km s}^{-1}$ . Only the part of evolutionary tracks corresponding to the evolutionary phase where  $X(\text{H}) \geq 0.4$  are plotted.

## 6.4. Wind properties

### 6.4.1. Mass-loss rates and filling factors

Clumping as considered in this paper is often referred to as micro-clumping because it assumes that the clumps are optically thin. The filling factors we derive cluster around  $f_{\infty} = 0.05$  with a fairly limited dispersion  $\pm 0.02$ . This corresponds to mass-loss rates reduced by factors of four to six compared to the homogeneous values that would be derived from fitting  $H\alpha$ . More interestingly, for all stars our mass-loss rates are within a factor of three of the predictions by Vink et al. (2000). Fig. 9 displays the ratio of predicted to measured mass-loss rates as a function of effective temperature. The ratios seem to increase with  $T_{\text{eff}}$  (the same trend is observed with luminosity). Theoretical mass-loss

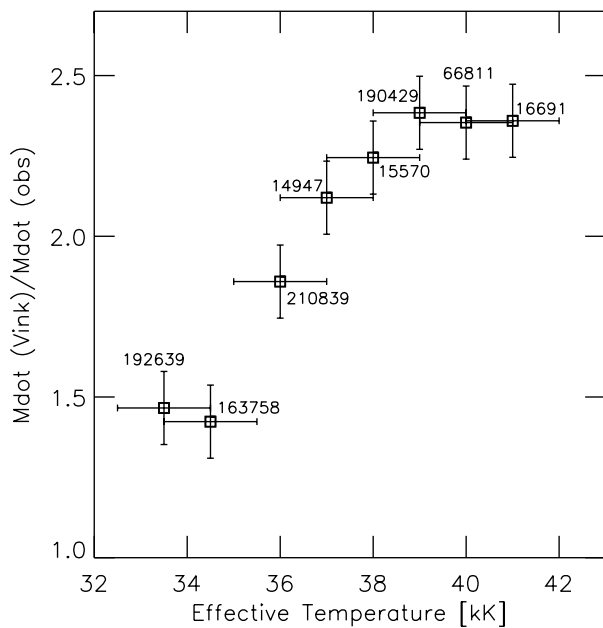


**Fig. 9.** Ratio of theoretical calculations by Vink et al. (2000) to measured mass-loss rates as function of effective temperature. Theoretical mass-loss rates are computed for the best-fit parameters for each star. The uncertainties in the ratios are estimated using error bars for measured  $\dot{M}$  only.

rates by Vink et al. (2000) decrease for decreasing effective temperature for fundamental stellar parameters typical of early-mid O-type supergiants. Therefore, Fig. 9 shows that the theoretical mass-loss rates increase more rapidly with  $T_{\text{eff}}$  (alternatively  $L$ ) than measured in the present sample.

As  $T_{\text{eff}}$  increases, the maximum of the flux distribution gradually shifts to shorter wavelengths, where more lines are available to contribute to the driving, thus increasing the mass-loss rates. The difference apparent in Fig. 9 suggests that more driving is present at higher  $T_{\text{eff}}$  in the theoretical calculations. However, we used a very large number of species and ions for our calculations of hydrodynamics in the models, at least as many as were included in Vink et al. (2000). Since mass-loss rates are mostly set by ions of the iron group, it is unlikely that we missed important lines that would instead be accounted for in the theoretical calculations by Vink et al. (2000).

Small-scale clumping significantly alters the ionization balance in the wind (Hillier 1991; Bouret et al. 2005). Depending on the temperature regime, dominant ions for different species might change, which could lead to a direct effect on the radiative driving. A recent study by Muijres et al. (2011) argued that the impact of clumping on the wind driving is an intricate function of the stellar temperature, the density inside the clumps and the physical size of the clumps. In the specific case of optically thin clumps, increased recombinations lead to an increase in the mass-loss rate, as a consequence of an increased line force. The amplitude of this effect is stronger as the clumping factor increases. This would be somewhat compensated for if porosity effects were included in their calculation, as a consequence of a decreased interaction between photons and the gas. All things considered, empirical mass-loss rates such as those we derived here cannot be reconciled as yet to those resulting from theoretical consideration, even including clumping corrections.

A promising alternative comes from the work by Lucy (2007, 2010a,b), who showed that turbulence in the photosphere reduces the wind driving force at the sonic point, thus strongly reducing the mass outflows, especially when compared to the calculations of Vink et al. (2000). Calculations were made in the microturbulence framework, because the nature and cause of the actual turbulence are unknown. It is expected that microturbulence should depend on the effective temperature, hence the reduction in mass-loss rates (relative to Vink et al. 2000) should be higher at higher  $T_{\text{eff}}$ , which might reduce the trend observed on Fig. 9.

Most likely, a proper description of stellar winds from massive stars should include optically thick clumps together with non-void interclump medium, and a non-monotonic velocity field (Sundqvist et al. 2011). This is especially important in accounting for velocity-porosity effects, which Sundqvist and collaborators conclude is especially relevant for resonance lines. Using a complex mixture of 1D radiation-hydrodynamics models to create 2D and 3D stochastic wind models, they computed synthetic line profiles for  $\lambda$  Cep, based on a Monte-Carlo radiative transfer code. They were able to reproduce the observed profiles of P v resonance lines and H $\alpha$  and to a lesser extent of He II  $\lambda$ 4686. They derived a mass-loss rate of  $1.5 \times 10^{-6} M_{\odot} \text{yr}^{-1}$ , which is much higher than the mass-loss that they would derive assuming optically thin clumps only ( $4. \times 10^{-7} M_{\odot} \text{yr}^{-1}$ ), although this last value is obtained from the fit to the P v resonance lines only.

The mass-loss rate we derive for  $\lambda$  Cep is very close to the one quoted by Sundqvist et al. (2011). Our fit to the wind lines is equally good when adopting lower-than-solar phosphorus abundance. Interestingly, both works fail to produce a double-peaked emission profile at He II  $\lambda$ 4686. It turns out that this specific shape, (as well as the absorption trough seen in H $\alpha$ ) is quite sensitive to the actual treatment of the rotation law in the wind. Sundqvist et al. (2011) had to adopt a fairly large amount of macro-clumping to reproduce the central absorption in H $\alpha$ . The extent to which a more proper treatment of the fast rotation of this star would change this conclusion is unclear. We will present models of  $\lambda$  Cep and  $\zeta$  Puppis including a realistic treatment of rotation in a forthcoming paper, but we argue at this step that this ingredient is as important as clumping (either optically thin or thick) to explain the observed shapes of H $\alpha$  and He II  $\lambda$ 4686 and that neglecting it leads to overemphasize the effect of (large-scale) clumping. At the same time the volume-filling factor approach slightly overestimates the strength of H $\alpha$  (Sundqvist et al. 2011). All in all,  $\lambda$  Cep might not be as representative of the influence of wind structures on emerging spectra as initially expected.

Clumping was found to start close to the photosphere in all but three stars out of sample, two of which are fast rotators. For the third one, namely HD 16691, we already mentioned that several emission profiles are characteristic of fast rotation, although not reflected by the  $v \sin i$ . We realize that the need to start clumping farther out in the wind is mostly driven by the need to fit the absorption trough seen in H $\alpha$  in the case of  $\zeta$  Puppis and  $\lambda$  Cep. Such a trough is not as clearly seen in HD 16691 (as  $\dot{M}$  is much higher) and the fit to N IV  $\lambda$ 1718 was the driver for the adopted  $v_{\text{cl}}$ . In any case, an accurate treatment of rotation is required for these objects to better investigate the actual properties of clumping.

## 6.4.2. Optically thin clumps and the P v problem

We showed in previous studies (Bouret et al. 2003; Hillier et al. 2003; Bouret et al. 2005) that the volume filling factor associated with wind clumping can be derived from the simultaneous fit to P v  $\lambda\lambda 1118-1128$ , O v  $\lambda 1376$ , N iv  $\lambda 1718$ , He ii  $\lambda 4686$ , and H $\alpha$ . The abundances for helium, nitrogen and oxygen were fixed from the analysis of photospheric lines; hence we had no other leverage but clumping and mass-loss rates to fit the wind lines listed above. The case of phosphorus is somewhat different because the FUV resonance doublet is the only available feature. Since the abundance of phosphorus is not expected to change over the lifetime of an individual star, a solar abundance should be appropriate. However, we had to use lower-than-solar phosphorus abundances, in addition to clumping, to improve the fit to P v resonance doublet. This result is reminiscent of our findings (see Hillier et al. 2003; Bouret et al. 2005) and although it might hint at a selective depletion of phosphorus in O supergiants with respect to the other metal abundances, it is also possibly related to the assumptions adopted to describe clumping in the models. The recent introduction of velocity porosity in radiative transfer calculations by Sundqvist et al. (2011) showed that the P v  $\lambda\lambda 1118-1128$  lines of  $\lambda$  Cep can be fitted with a solar abundance of phosphorus. We note in this context that these lines in HD 163758 do not reflect the ratio of oscillator strengths of the two lines, thus indicating that these lines are saturated. Prinja & Massa (2010) concluded from their study of Si iv  $\lambda\lambda 1393-1403$  on a sample of B supergiants that velocity porosity could explain this behavior. HD 163758 is therefore a very good candidate to investigate a more realistic treatment of wind inhomogeneities for O supergiants.

The primary consequence of being forced to reduce the phosphorus abundance in CMFGEN models is to change the radial optical depth of the resonance lines, hence their strength. Since the optical depth of the wind in one line is related to the ionization fraction of the corresponding ion ( $\tau_{rad} \propto \dot{M} q_i A_E$  with  $A_E$  and  $q_i$  the abundance of element E and its ionization fraction for stage i), the need to decrease the phosphorus abundance compared to solar could be related to the incorrect determination of the wind ionization (i.e., over-production of the P<sup>+</sup> ion). To investigate the problem of phosphorus ionization in more details, we derived an empirical  $\dot{M}q(P^{+4})$  by profile fitting using the Sobolev with exact integration (SEI) method (Lamers et al. 1987). We refer to Massa et al. (2003) for a detailed presentation of the method. We used wind quantities such as  $v_\infty$  and  $\beta$  from the spectroscopic study (Table 3). Figure 10 compares the  $\dot{M}q(P^{+4})$  derived with this approach to those from the modeling with CMFGEN. Overall, the agreement between the quantities from both techniques is very satisfactory when a reduced phosphorus abundance is used. In other words, in this case only, very similar optical depths are derived, while when  $P = P_\odot$  is used, the optical depths from CMFGEN are too high. Although the global scaling with  $P/P_\odot \leq 1$  improves the agreement, a clear trend for too high  $\dot{M}q(P^{+4})$  in CMFGEN is observed at high velocities (typically above  $v/v_\infty \geq 0.7$ ) for all but one star. The fit (Appendix A) shows that the synthetic CMFGEN profiles are indeed too strong in absorption near the blue-edge of the absorption components of the P Cygni profiles of P v lines<sup>5</sup>. This divergence between  $\dot{M}q(P^{+4})$  from CMFGEN and SEI is stronger

<sup>5</sup>  $\zeta$  Puppis shows by far the largest disagreement for empirical and theoretical  $\dot{M}q(P^{+4})$ , which also translates to the poorest fit to the observations within the sample. The clear peak in the SEI  $\dot{M}q(P^{+4})$  distribution between  $0.6 \leq v/v_\infty \leq 0.7$  might indicate the presence of a DAC in the wind of the star at the time of the observation

for stars hotter than 36,000 K. It indicates that the ionization fraction of q(P<sup>+</sup>) is predicted too high in CMFGEN in the outer part of the winds. The ionization fraction of P<sup>+</sup> in our models shows that P v is a dominant ion below  $0.5v_\infty$  for all stars, consistent with results in Fullerton et al. (2006) and Kr̄t̄icka & Kub̄at (2009). In stars with  $T_{eff} \geq 37,000$  K, P v remains the dominant phosphorus ion throughout the wind.

Sundqvist et al. (2011) suggested that X-rays have a significant influence on the ionization in the outer part of the winds. We performed several tests with different X-ray fluxes for these stars. We did not find a significant influence of X-ray radiation on the ionization of phosphorus, unless very high X-ray fluxes were used, which would alter the ionization of other species as well. Such very high X-ray fluxes provides a “tail” of XUV radiation that is strong enough to alter the P v ionization fraction but the corresponding (emitted)  $\log L_X/L_{bol}$  are not consistent with the now well-defined relation (Sana et al. 2007). We note that Kr̄t̄icka & Kub̄at (2009) already concluded that X-ray radiation alone cannot change the ionization fraction of P v significantly enough to avoid  $\dot{M}$  reduction when clumping is taken into account.

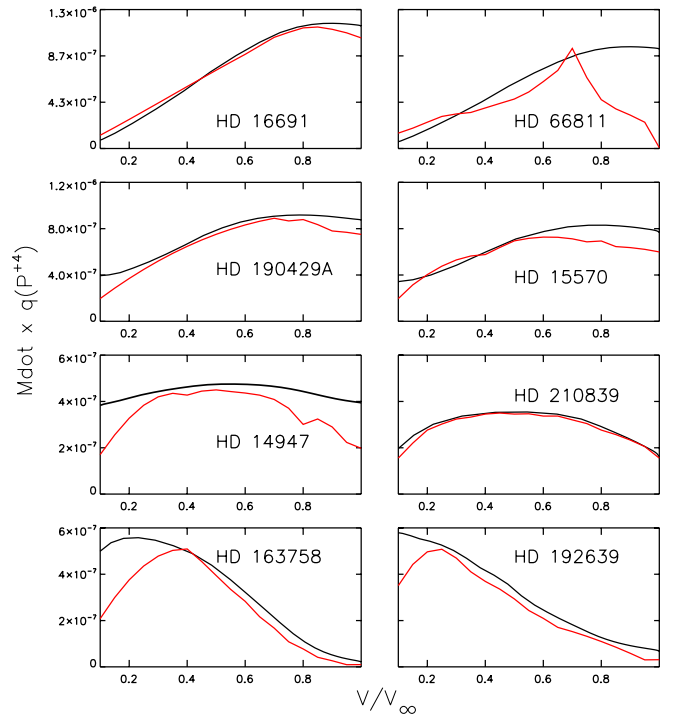


**Fig. 10.**  $\dot{M}q(P^{+4})$  as a function of normalized velocity derived from the modeling with CMFGEN (black) or from SEI (red).

On the other hand, Waldron & Cassinelli (2010) concluded that strong wind XUV-EUV emission line radiation could alter the ionization fraction of P v, while remaining compatible with observational constraints. Nevertheless, other important questions such as photoionizations from excited states, influence of other species and optical depth effects in the He ii continuum that might challenge their conclusion are ignored.

Our fits to the P v  $\lambda\lambda 1118-1128$  resonance lines are very satisfactory, given the relative simplicity of the adopted treatment of clumping. Again, the adopted phosphorus abundance is lower than solar but we seem to need the same  $P/P_\odot = 0.5 \pm 0.2$  ratio for all stars, which we can adopt as a fiducial value for subsequent modeling of other early-type supergiants. We believe

that wind parameters as derived from the present study, by fitting several wind profiles over a range of species and ionization stages provide a realistic and robust description of the stellar winds. Nevertheless, more consistent descriptions of wind clumping will need to be considered in future modeling. The velocity porosity presented by Sundqvist et al. (2011) is promising, although the velocity structure of the hydrodynamic models do not exhibit the porosity in velocity space that is required to produce the observed P-Cygni profile shapes, and reconcile H $\alpha$  and UV mass-loss rates. Other important questions will need to be addressed, including a self-consistent calculation of the ionization structure, the extension to optically thick winds, and a realistic description (as yet lacking) of the structure of stellar winds.

### 6.5. Line force consistency check

Since CMFGEN computes the full radiation field, we can accurately compute the radiative force. Consequently, we can check whether the derived radiative force is consistent with that needed to drive the wind. For convenience we write the momentum equation as

$$g_{rad} = v \frac{dv}{dr} + \frac{1}{\rho} \frac{dP_g}{dr} + g \quad (4)$$

where  $P_g$  is the gas pressure,  $v$  is the velocity,  $g = GM/r^2$ , and  $g_{rad}$  is the total radiative force, which is evaluated using

$$g_{rad} = \frac{\chi_f L}{4\pi c r^2}, \quad (5)$$

where  $\chi_f$  is the flux mean opacity.

If the mass-loss rate, velocity law, and gravity in our models are consistent, the left-hand-side (LHS) of Eq. 4 should be the same as the right-hand-side (RHS). In Fig. 11 we compare the LHS and RHS for a model similar to that found for  $\zeta$  Puppis:  $T_{\text{eff}}=41,000$  K,  $\dot{M} = 1.7 \times 10^{-6} M_{\odot} \text{ yr}^{-1}$ , and  $f_{\infty} = 0.05$  (which can be compared to our best-fit model of  $T_{\text{eff}}=40,000$  K,  $\dot{M} = 2.0 \times 10^{-6} M_{\odot} \text{ yr}^{-1}$ , and  $f_{\infty} = 0.05$ ). As is readily apparent, our line force is too strong in most of the wind, indicating that the velocity law is incorrect, or more likely, the mass-loss rate is too low. The same conclusion is reached if we use the parameters found for the best-fit  $\zeta$  Puppis model.

The simplest means of obtaining better consistency between the LHS and RHS would be to increase the mass-loss rate, and the simplest way of maintaining ‘‘consistency’’ with the spectral fit would be to simultaneously increase the volume filling factor  $f$ . As expected, tests show that a moderate increase in the mass-loss rate to  $2.7 \times 10^{-6} M_{\odot} \text{ yr}^{-1}$  and  $f_{\infty} = 0.1$  yields a much better agreement. As discussed previously, a slightly higher  $f$  value might give consistent spectral fits if the effects of velocity porosity were taken into account.

Because we can perform this consistency check, we could, in principle, use the wind dynamics to derive an additional constraint on  $\dot{M}$ . However, there are several difficulties involved. First, it is very difficult to obtain agreement between the LHS and RHS around the sonic point ( $v \sim 20 \text{ km s}^{-1}$ ) – this is not surprising, since the critical point lies near the sonic point. We can only obtain a moderate agreement if we adopt a low microturbulent velocity of  $5 \text{ km s}^{-1}$ , a value which is inconsistent with that required to fit the Fe lines in the UV, and with that generally inferred for O supergiants. Understanding the nature of this microturbulence is of crucial importance for understanding radiation driven winds. Moreover, we found it easier to achieve a fit

when  $\beta < 1$  in this region, a value more in line with the predictions of radiation-driven wind theory. Second, there is increasing evidence that winds are clumped and dynamic - not steady-state as assumed by Eq. 4. Therefore, for full consistency, we need to run hydrodynamic simulations, and since  $\zeta$  Puppis is a rapid rotator, this may necessitate 3D simulations. Third, there is the problem of velocity porosity, which will tend to reduce the line force for a given mass-loss rate and clumping. Fourth, we need to simultaneously reduce the abundances, because mass-loss rates are predicted to scale as  $Z^{0.85}$  (Vink et al. 2001). A systematic error in the abundances by a factor of 1.5 (which is not unrealistic) will cause a  $\sim 40\%$  error in  $\dot{M}$ . Consequently, while we can conclude that the spectroscopically derived mass-loss rates, and the mass-loss rate inferred from the line force, are consistent to within a factor of 2 for  $\zeta$  Puppis, it is almost impossible to obtain better consistency at the present time. It is also worth noting that it is necessary to include Ne, S, Ar, Cl etc. in the model calculations. While they do not have a major influence on the observed spectrum, they do significantly enhance the radiative line force in the wind.

In general, the derived spectroscopic mass-loss rates, and those inferred from the dynamics for O supergiant agree reasonably well. The same is not true for dwarf O stars, where the derived CMFGEN line force indicates a much higher mass-loss rate than that derived spectroscopically from the weak UV P Cygni profiles (e.g., Martins et al. 2012).

## 7. Conclusions

We have modeled the FUV-UV and optical spectra of a sample of eight O-type supergiants to investigate their surface abundances and wind properties. The results that we obtained can be summarized as follows:

- Supergiants with spectral types between O4 to O7.5 order along a well-defined evolutionary sequence, in terms of ages and masses, from younger and more massive to older stars with lower initial masses. O4 supergiants cluster around the 3 Myr isochrone and are more massive than  $60 M_{\odot}$ , while from O5 to O7.5, stars have masses in the range  $50 - 40 M_{\odot}$  and are  $4 \pm 0.3$  Myr old. No mass-discrepancy is observed since spectroscopic and evolutionary masses agree within the uncertainties (and in any case within 20%). Despite the high signal-to-noise ratios that can be achieved, the use of echelle spectra compromises the rectification of spectra, especially in the vicinity of the broad H lines that are the primary diagnostics of  $\log g$ . Improving  $\log g$  determinations is crucial for determining stellar masses by spectroscopic methods.
- All stars exhibit significant enrichment of nitrogen, as expected from their evolutionary status. Carbon is depleted with respect to an initial abundance assumed to be solar-like for all but one star, namely HD 163758. This star turned out to be carbon-rich (twice solar at least) as expected from its spectral classification. If depleted by the amount expected on the basis of its evolutionary status, its initial carbon abundance was likely very high. All other stars have either a nitrogen enrichment that is too low for the measured carbon depletion, or alternatively too strong a carbon depletion for the measured nitrogen enrichment.
- The observed carbon and nitrogen mass-fractions are compatible with those expected from the models, for the measured stellar masses. On the other hand, the N/C ratios as a function of age are inconsistent with the theoretical predictions for the four earliest (O4 spectral type) stars of the



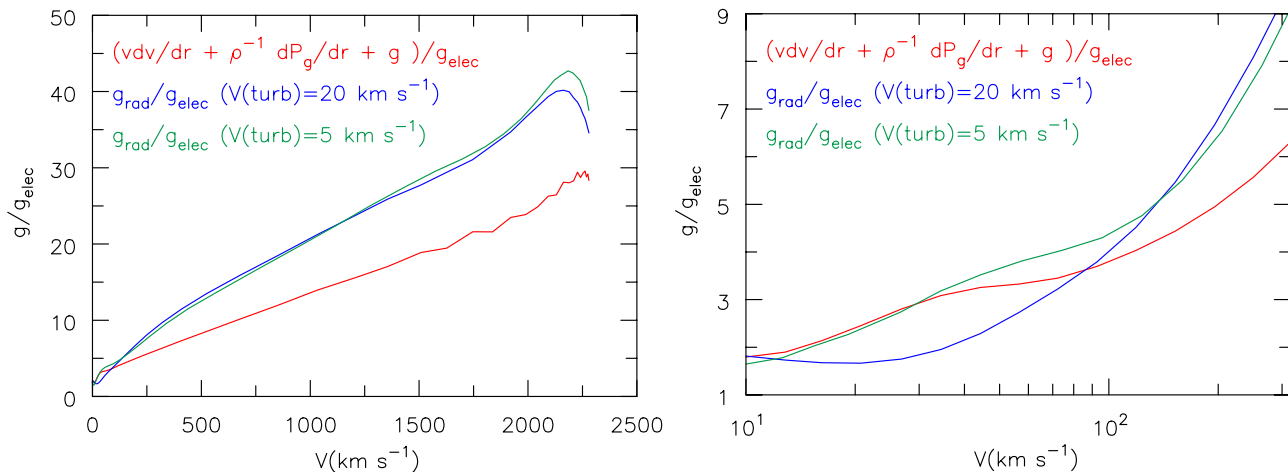


**Fig. 11.** Illustration comparing the radiative line force with other terms in the momentum equation. The model parameters are similar to those of  $\zeta$  Puppis;  $T_{\text{eff}}=41,000$  K and  $M_{\odot}=1.7 \times 10^{-6} M_{\odot} \text{yr}^{-1}$ . The right-hand plot illustrates the sensitivity of the line force to the adopted microturbulent velocity around the sonic point. Below  $10 \text{ km s}^{-1}$  hydrostatic equilibrium is valid.

sample. The efficiency of rotational mixing as a function of age is questioned for these stars. Other mechanisms might be needed to explain the observed patterns. A solution could be that the observed metallicity gradient within the galactic disk should be taken into account rather than assuming standard solar values for metals. Alternatively, a modified efficiency of mixing may be needed in stellar evolution models.

- Mass-loss rates derived using clumped models are lower than theoretical predictions by factors that range from 1.5 to 2.5. This difference is actually very reasonable given the known uncertainty on both estimates. The corresponding filling-factors associated with small-scale clumping are  $0.05 \pm 0.02$ . Clumping is found to start close to the photosphere for all but three stars, two of which are fast rotators, namely  $\lambda$  Cep and  $\zeta$  Puppis. Although its  $v \sin i$  is smaller, HD 16691 behaves like these two fast rotators; several optical lines indicate that this star could indeed be a fast rotator as well, seen at a higher inclination.
- The ratios of theoretical to observed mass-loss rates increase with luminosity (or  $T_{\text{eff}}$ ), which suggests that too much driving might be present in the models for the hotter and more massive stars. We found no convincing explanation for this behavior at this point. The need for a sub-solar phosphorus abundance to fit the P v resonance line was investigated. Overall, empirical ionization fractions derived within the SEI framework agree well with the theoretical fractions from CMFGEN. Some remaining discrepancies are observed, especially in the outer regions of the winds (higher radial velocities). P v is predicted to be overabundant by CMFGEN in these circumstances. In any case, sub-solar phosphorus abundance are needed to artificially decrease the radial optical depth of the P v lines. Although this problem is directly related to the micro-clumping framework we work with, the needed abundance reduction is fairly constant and could be adopted as default for future work.

To reach a more complete, more quantitative, understanding of the observed trends of the photospheric and wind properties for Galactic supergiants, we will extend our analysis to later spectral types (down to the end of the O-type stars sequence). In forthcoming papers, we will also explore the different technical problems we met during the present analysis, such as the formation of excited lines of CNO elements that are fundamental for

an abundance analysis; and the extent to which incorporating rotation improves fits to key diagnostic features in the spectra of massive stars.

*Acknowledgements.* We thank the referee, Sergio Simón-Díaz, for useful comments and suggestions. We also thank Selma de Mink for fruitful discussions about stellar evolution and abundances. This research has made use of the SIMBAD database, operated at CDS, Strasbourg, France. We want to acknowledge the valuable help of Hugues Sana with the *FEROS* data of  $\zeta$  Puppis. STScI is operated by the Association of Universities for Research in Astronomy, Inc., under NASA contract NAS5-26555. Support for MAST for non-HST data is provided by the NASA Office of Space Science via grant NAG5-7584 and by other grants and contracts. J.-C. Bouret is indebted to George Sonneborn for his invitation to work at NASA/GSFC during the completion of this work. We thank the French Agence Nationale de la Recherche (ANR) for financial support. D. J. Hillier acknowledges support from STScI theory grant HST-AR-11756.01.A and from NASA ADP Grant: NNG04GC81G.

## References

- Aerts, C., Puls, J., Godart, M., & Dupret, M.-A. 2009, *A&A*, 508, 409  
 Allard, N., Le Dourneuf, M., Artru, M.-C., & Lanz, T. 1991, *A&AS*, 91, 399  
 Asplund, M., Grevesse, N., & Sauval, A. 2005, in *ASP Conf. Ser.*, Vol. 336, *Cosmic Abundances as Records of Stellar Evolution and Nucleosynthesis*, ed. T.G. Barnes III & F.N. Bash (San Francisco: ASP), 25  
 Bagnulo, S., Jehin, E., Ledoux, C., et al. 2003, *The Messenger*, 114, 10  
 Baranne, A., Queloz, D., Mayor, M., et al. 1996, *A&AS*, 119, 373  
 Bianchi, L. & Garcia, M. 2002, *ApJ*, 581, 610  
 Bouret, J.-C., Lanz, T., & Hillier, D. J. 2005, *A&A*, 438, 301  
 Bouret, J.-C., Lanz, T., Hillier, D. J., et al. 2003, *ApJ*, 595, 1182  
 Bromm, V., Coppi, P. S., & Larson, R. B. 1999, *ApJ*, 527, L5  
 Busche, J. R. & Hillier, D. J. 2005, *AJ*, 129, 454  
 Cardelli, J. A., Clayton, G. C., & Mathis, J. S. 1989, *ApJ*, 345, 245  
 Cassinelli, J. P. & Olson, G. L. 1979, *ApJ*, 229, 304  
 Conti, P. S. & Bohannan, B. 1989, in *Astrophysics and Space Science Library*, Vol. 157, *IAU Colloq. 113: Physics of Luminous Blue Variables*, ed. K. Davidson, A. F. J. Moffat, & H. J. G. L. M. Lamers, 297–+  
 Conti, P. S., Hanson, M. M., Morris, P. W., Willis, A. J., & Fossey, S. J. 1995, *ApJ*, 445, L35  
 Cranmer, S. R. & Owocki, S. P. 1996, *ApJ*, 462, 469  
 Crowther, P. A., Hillier, D. J., Abbott, J. B., & Fullerton, A. W. 2002, *A&A*, 392, 653  
 Cunha, K., Hubeny, I., & Lanz, T. 2006, *ApJ*, 647, L143  
 De Becker, M., Rauw, G., & Linder, N. 2009, *ApJ*, 704, 964  
 De Becker, M., Rauw, G., Manfroid, J., & Eenens, P. 2006, *A&A*, 456, 1121  
 de Mink, S. E., Langer, N., & Izzard, R. G. 2011, *Bulletin de la Societe Royale des Sciences de Liege*, 80, 543  
 Dessart, L. & Owocki, S. P. 2003, *A&A*, 406, L1  
 Dessart, L. & Owocki, S. P. 2005, *A&A*, 437, 657  
 Domiciano de Souza, A., Kervella, P., Jankov, S., et al. 2003, *A&A*, 407, L47

- Donati, J.-F., Semel, M., Carter, B. D., Rees, D. E., & Collier Cameron, A. 1997, *MNRAS*, 291, 658
- Eversberg, T., Lepine, S., & Moffat, A. F. J. 1998, *ApJ*, 494, 799
- Fullerton, A. W., Massa, D. L., & Prinja, R. K. 2006, *ApJ*, 637, 1025
- Gómez, D. O. & Niemela, V. S. 1987a, *Revista Mexicana de Astronomía y Astrofísica*, vol. 14, 14, 293
- Gómez, D. O. & Niemela, V. S. 1987b, *Revista Mexicana de Astronomía y Astrofísica*, vol. 14, 14, 293
- Hamann, W.-R., Feldmeier, A., & Oskinova, L. M., eds. 2008, *Clumping in hot-star winds* (Potsdam: Universitätsverlag Potsdam)
- Harries, T. J. 2000, *MNRAS*, 315, 722
- Heap, S. R., Lanz, T., & Hubeny, I. 2006, *ApJ*, 638, 409
- Heger, A. & Langer, N. 2000, *ApJ*, 544, 1016
- Herrero, A., Kudritzki, R. P., Vilchez, J. M., et al. 1992, *A&A*, 261, 209
- Hillier, D. J. 1988, *ApJ*, 327, 822
- Hillier, D. J. 1989, *ApJ*, 347, 392
- Hillier, D. J. 1991, *A&A*, 247, 455
- Hillier, D. J., Lanz, T., Heap, S. R., et al. 2003, *ApJ*, 588, 1039
- Hillier, D. J. & Miller, D. L. 1998, *ApJ*, 496, 407
- Hjorth, J., Sollerman, J., Møller, P., et al. 2003, *Nature*, 423, 847
- Howarth, I. D. & Prinja, R. K. 1996, *Ap&SS*, 237, 125
- Howarth, I. D., Prinja, R. K., & Massa, D. 1995, *ApJ*, 452, L65
- Hubeny, I. & Lanz, T. 1995, *ApJ*, 439, 875
- Hunter, I., Brott, I., Langer, N., et al. 2009, *A&A*, 496, 841
- Hunter, I., Brott, I., Lennon, D. J., et al. 2008, *ApJ*, 676, L29
- Hunter, I., Dufton, P. L., Smartt, S. J., et al. 2007, *A&A*, 466, 277
- Kaper, L., Henrichs, H. F., Fullerton, A. W., et al. 1997, *A&A*, 327, 281
- Krtićka, J. & Kubát, J. 2009, *MNRAS*, 394, 2065
- Lamers, H. J. G. L. M., Cerruti-Sola, M., & Perinotto, M. 1987, *ApJ*, 314, 726
- Langer, N., Cantiello, M., Yoon, S.-C., et al. 2008, in *IAU Symposium*, Vol. 250, IAU Symposium, ed. F. Bresolin, P. A. Crowther, & J. Puls, 167–178
- Lanz, T. & Hubeny, I. 2003, *ApJS*, 146, 417
- Laughlin, C. 1990, *Phys. Scr.*, 42, 551
- Lucy, L. B. 2007, *A&A*, 468, 649
- Lucy, L. B. 2010a, *A&A*, 524, A41+
- Lucy, L. B. 2010b, *A&A*, 512, A33+
- Lucy, L. B. & Solomon, P. M. 1970, *ApJ*, 159, 879
- Maeder, A. & Meynet, G. 2000, *ARA&A*, 38, 143
- Maeder, A. & Meynet, G. 2001, *A&A*, 373, 555
- Maeder, A., Meynet, G., Ekström, S., & Georgy, C. 2009, *Communications in Asteroseismology*, 158, 72
- Maíz-Apellániz, J., Walborn, N. R., Galué, H. Á., & Wei, L. H. 2004, *ApJS*, 151, 103
- Markova, N. 2002, *A&A*, 385, 479
- Markova, N., Puls, J., Repolust, T., & Markov, H. 2004, *A&A*, 413, 693
- Markova, N., Puls, J., Scuderi, S., & Markov, H. 2005, *A&A*, 440, 1133
- Martins, F. & Hillier, D. J. 2012, in preparation
- Martins, F., Hillier, D. J., Paumard, T., et al. 2008, *A&A*, 478, 219
- Martins, F., Mahy, L., Hillier, D. J., & Rauw, G. 2012, *A&A*, 538, A39
- Martins, F. & Plez, B. 2006, *A&A*, 457, 637
- Martins, F., Pomarès, M., Deharveng, L., Zavagno, A., & Bouret, J. C. 2010, *A&A*, 510, A32
- Martins, F., Schaerer, D., & Hillier, D. J. 2005, *A&A*, 436, 1049
- Mason, B. D., Gies, D. R., Hartkopf, W. I., et al. 1998, *AJ*, 115, 821
- Massa, D., Fullerton, A. W., Nichols, J. S., et al. 1995, *ApJ*, 452, L53
- Massa, D., Fullerton, A. W., Sonneborn, G., & Hutchings, J. B. 2003, *ApJ*, 586, 996
- Massey, P., Johnson, K. E., & Degioia-Eastwood, K. 1995, *ApJ*, 454, 151
- Meynet, G., Eggenberger, P., & Maeder, A. 2011, *A&A*, 525, L11
- Meynet, G. & Maeder, A. 2003, *A&A*, 404, 975
- Meynet, G. & Maeder, A. 2005, *A&A*, 429, 581
- Meynet, G. & Maeder, A. 2007, *A&A*, 464, L11
- Mihalas, D., Hummer, D. G., & Conti, P. S. 1972, *ApJ*, 175, L99+
- Morton, D. C. & Underhill, A. B. 1977, *ApJS*, 33, 83
- Muijres, L. E., de Koter, A., Vink, J. S., et al. 2011, *A&A*, 526, A32
- Najarro, F., Hanson, M. M., & Puls, J. 2011, *A&A*, 535, A32
- Najarro, F., Hillier, D. J., Puls, J., Lanz, T., & Martins, F. 2006, *A&A*, 456, 659
- Nakamura, F. & Umemura, M. 1999, *ApJ*, 515, 239
- Nieva, M.-F. & Przybilla, N. 2012, *A&A*, 539, A143
- Nieva, M.-F. & Simón-Díaz, S. 2011, *A&A*, 532, A2
- Oskinova, L. M. 2005, *MNRAS*, 361, 679
- Oskinova, L. M., Hamann, W.-R., & Feldmeier, A. 2007, *A&A*, 476, 1331
- Owocki, S. P. 1994, *Ap&SS*, 221, 3
- Owocki, S. P. 2008, in *Clumping in Hot-Star Winds*, ed. W.-R. Hamann, A. Feldmeier, & L. M. Oskinova, 121
- Owocki, S. P., Castor, J. I., & Rybicki, G. B. 1988, *ApJ*, 335, 914
- Owocki, S. P. & Puls, J. 1999, *ApJ*, 510, 355
- Pauldrach, A. W. A., Kudritzki, R. P., Puls, J., Butler, K., & Hunsinger, J. 1994, *A&A*, 283, 525
- Pauldrach, A. W. A., Vanbeveren, D., & Hoffmann, T. L. 2012, *A&A*, 538, A75
- Prinja, R. K. & Fullerton, A. W. 1994, *ApJ*, 426, 345
- Prinja, R. K., Markova, N., Scuderi, S., & Markov, H. 2006, *A&A*, 457, 987
- Prinja, R. K. & Massa, D. L. 2010, *A&A*, 521, L55+
- Przybilla, N., Firnstein, M., Nieva, M. F., Meynet, G., & Maeder, A. 2010, *A&A*, 517, A38+
- Przybilla, N., Nieva, M., & Butler, K. 2008, *ApJ*, 688, L103
- Puls, J., Kudritzki, R.-P., Herrero, A., et al. 1996, *A&A*, 305, 171
- Puls, J., Markova, N., Scuderi, S., et al. 2006, *A&A*, 454, 625
- Rauw, G., Morrison, N. D., Vreux, J., Gosset, E., & Mulliss, C. L. 2001, *A&A*, 366, 585
- Repolust, T., Puls, J., Hanson, M. M., Kudritzki, R.-P., & Mokiem, M. R. 2005, *A&A*, 440, 261
- Repolust, T., Puls, J., & Herrero, A. 2004, *A&A*, 415, 349
- Rivero González, J. G., Puls, J., & Najarro, F. 2011, *A&A*, 536, A58
- Runacres, M. C. & Owocki, S. P. 2002, *A&A*, 381, 1015
- Runacres, M. C. & Owocki, S. P. 2005, *A&A*, 429, 323
- Sahnow, D. J., Moos, H. W., Ake, T. B., et al. 2000, *ApJ*, 538, L7
- Sahu, M. & Blaauw, A. 1993, in *ASP Conf. Ser.*, Vol. 35, *Massive Stars: Their Lives in the Interstellar Medium*, ed. J. P. Cassinelli & E. B. Churchwell (San Francisco: ASP), 278
- Sana, H. & Evans, C. J. 2011, in *IAU Symposium*, Vol. 272, *IAU Symposium*, ed. C. Neiner, G. Wade, G. Meynet, & G. Peters, 474–485
- Sana, H., Rauw, G., Sung, H., Gosset, E., & Vreux, J.-M. 2007, *MNRAS*, 377, 945
- Schilbach, E. & Röser, S. 2008, *A&A*, 489, 105
- Simón-Díaz, S. 2010, *A&A*, 510, A22+
- Simón-Díaz, S. & Herrero, A. 2007, *A&A*, 468, 1063
- Smith, N. & Owocki, S. P. 2006, *ApJ*, 645, L45
- Sota, A., Maíz Apellániz, J., Walborn, N. R., et al. 2011, *ApJS*, 193, 24
- Steidel, C. C., Gialvalisco, M., Pettini, M., Dickinson, M., & Adelberger, K. L. 1996, *ApJ*, 462, L17+
- Sundqvist, J. O., Puls, J., & Feldmeier, A. 2010, *A&A*, 510, A11+
- Sundqvist, J. O., Puls, J., Feldmeier, A., & Owocki, S. P. 2011, *A&A*, 528, A64+
- Torres, A. V., Conti, P. S., & Massey, P. 1986, *ApJ*, 300, 379
- Turner, N. H., ten Brummelaar, T. A., Roberts, L. C., et al. 2008, *AJ*, 136, 554
- Villamariz, M. R. & Herrero, A. 2000, *A&A*, 357, 597
- Vink, J. S., de Koter, A., & Lamers, H. J. G. L. M. 2000, *A&A*, 362, 295
- Vink, J. S., de Koter, A., & Lamers, H. J. G. L. M. 2001, *A&A*, 369, 574
- Walborn, N. 2001, in *ASP Conf. Ser.*, Vol. 242, *Eta Carinae and Other Mysterious Stars: The Hidden Opportunities of Emission Spectroscopy*, ed. T. R. Gull, S. Johansson, & K. Davidson (San Francisco: ASP), 217
- Walborn, N. R. 1971a, *ApJ*, 167, 357
- Walborn, N. R. 1971b, *ApJS*, 23, 257
- Walborn, N. R. 1973, *AJ*, 78, 1067
- Walborn, N. R. & Howarth, I. D. 2000, *PASP*, 112, 1446
- Walborn, N. R., Sota, A., Maíz Apellániz, J., et al. 2010, *ApJ*, 711, L143
- Waldron, W. L. & Cassinelli, J. P. 2010, *ApJ*, 711, L30
- Woosley, S. E. & Bloom, J. S. 2006, *ARA&A*, 44, 507
- Yoon, S. & Langer, N. 2005, *A&A*, 443, 643
- Zavagno, A., Pomarès, M., Deharveng, L., et al. 2007, *A&A*, 472, 835
- Zsargó, J., Hillier, D. J., Bouret, J., et al. 2008, *ApJ*, 685, L149
- Zsargó, J., Hillier, D. J., & Georgiev, L. N. 2006, *A&A*, 447, 1093

## **Appendix A: Best fits**

In this appendix we present our best-fit models to the optical and UV spectra for the eight stars in our sample. The wavelength range between 1200 and 1225 Å was not used in the spectral analysis since it suffers from a strong interstellar Lyman absorption. Nevertheless, we take this interstellar absorption into account by adding the effects of a representative hydrogen column density to our synthetic spectra in our final plots.



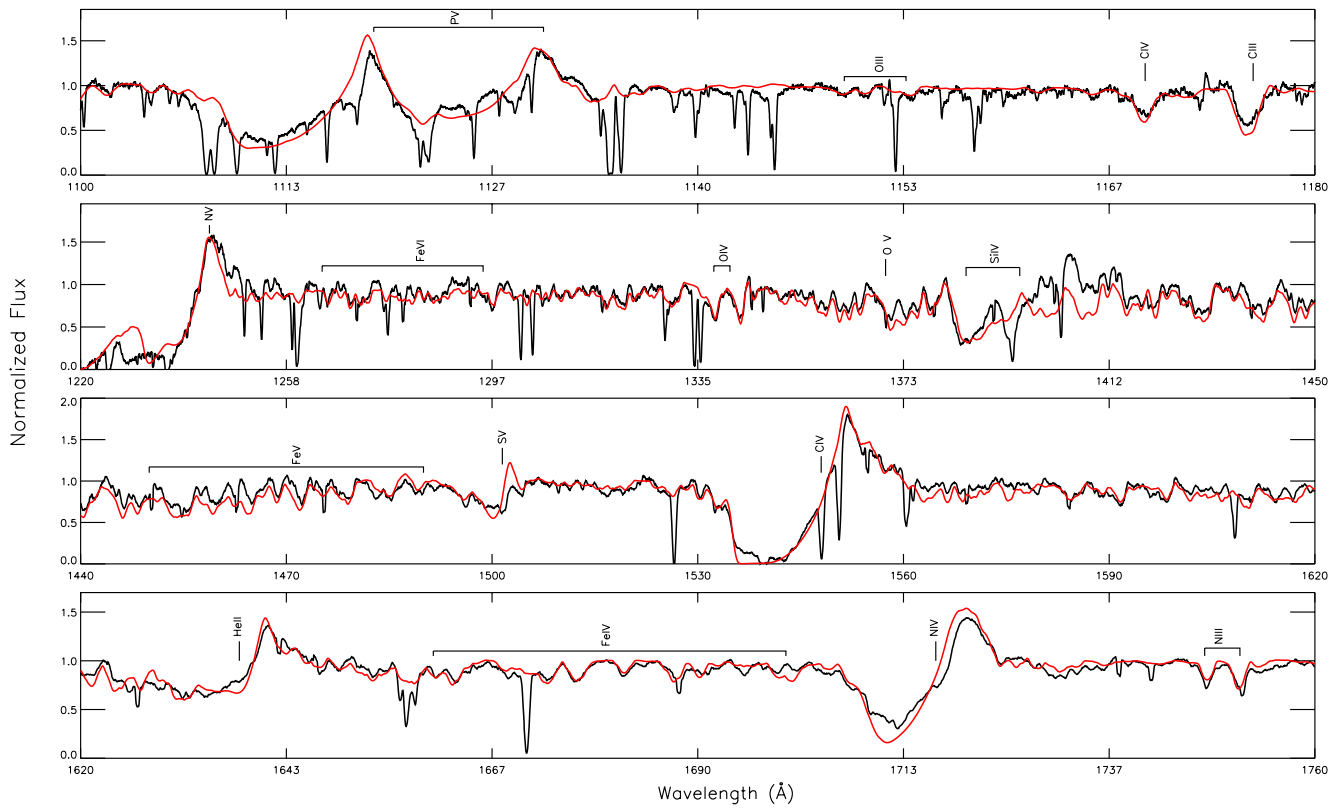


**Fig. A.1.** Best-fit model for HD 190429A (red line) compared to *FUSE* and *IUE* spectra (black line)

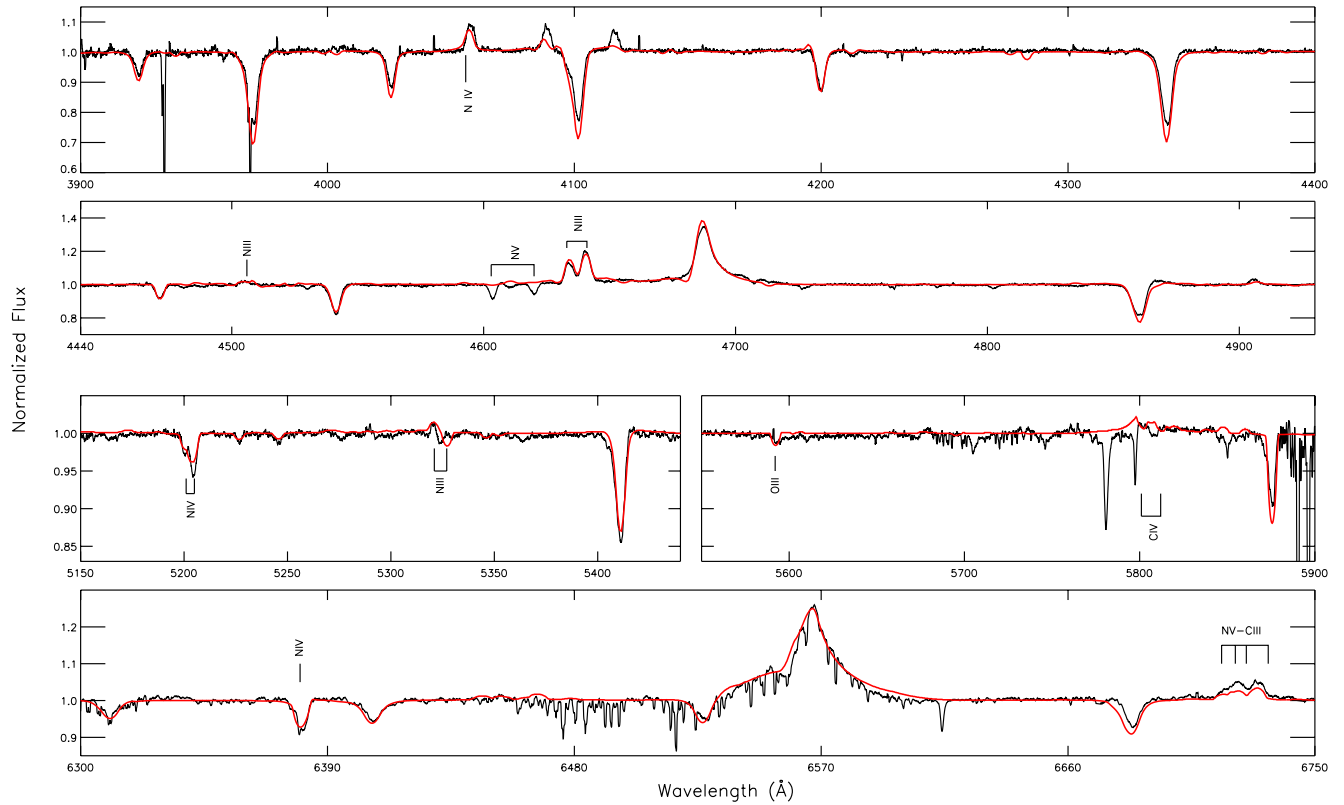


**Fig. A.2.** Best-fit model for HD 190429A (red line) compared to the *ELODIE* spectrum (black line)

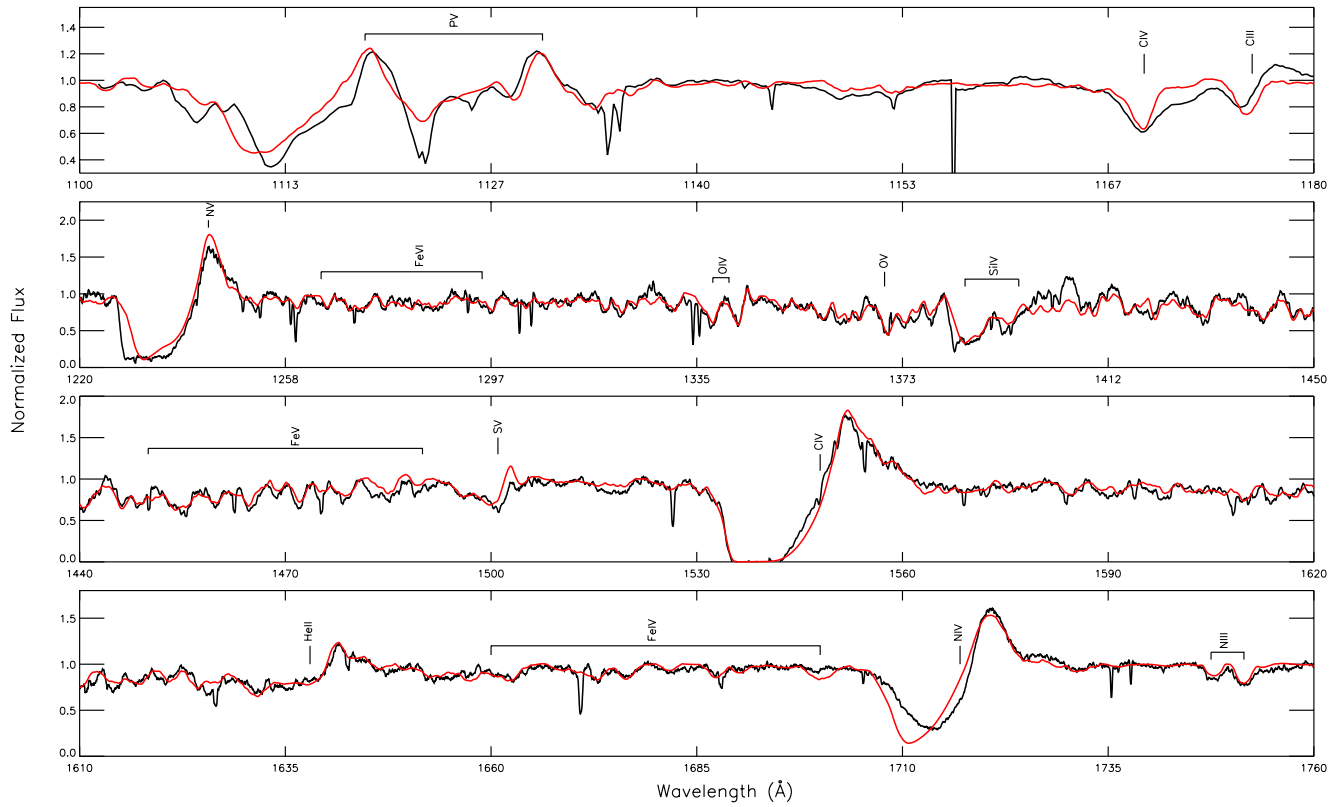


**Fig. A.3.** Best-fit model for HD 66811 (red line) compared to *Copernicus* and *IUE* spectra (black line)

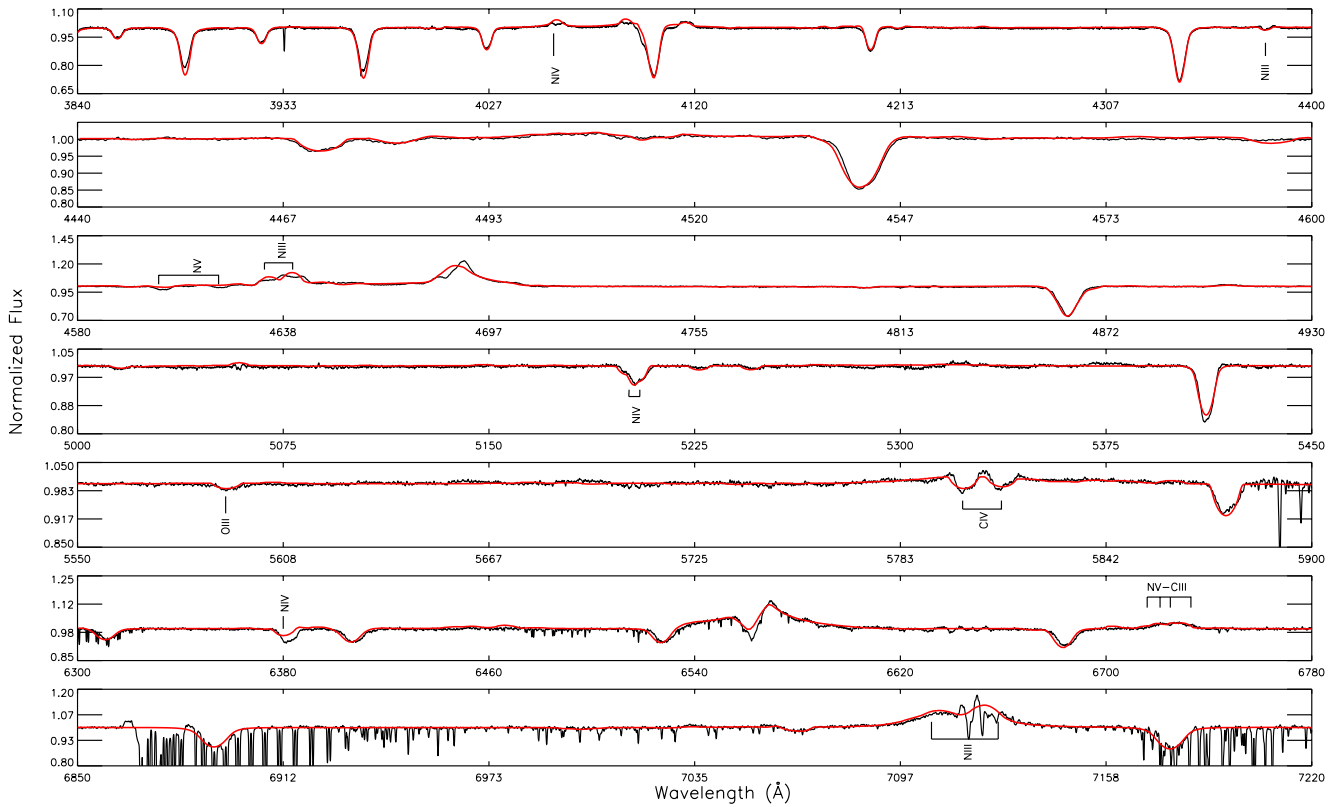


**Fig. A.4.** Best-fit model for HD 66811 (red line) compared to the *FEROS* spectrum (black line)

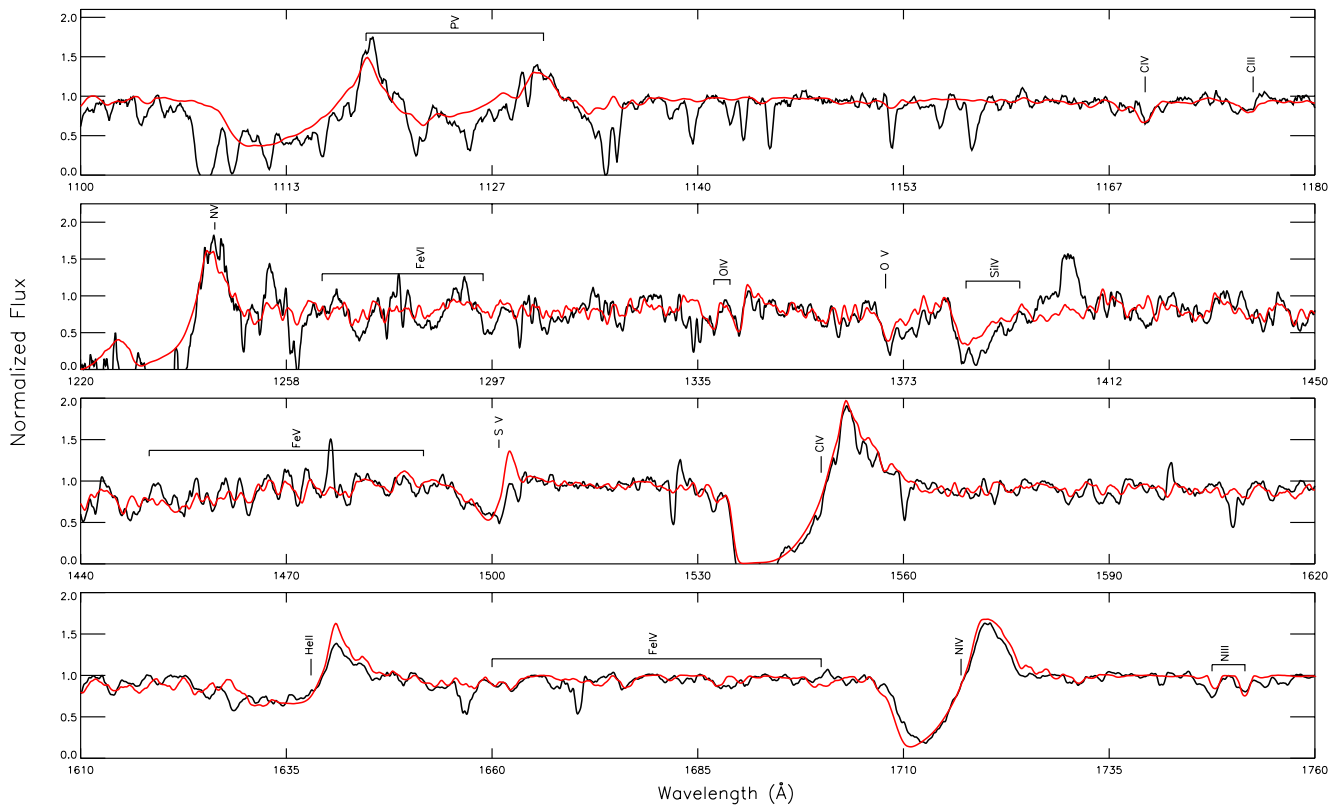


**Fig. A.5.** Best-fit model for HD 16691 (red line) compared to *FUSE* and *IUE* spectra (black line)

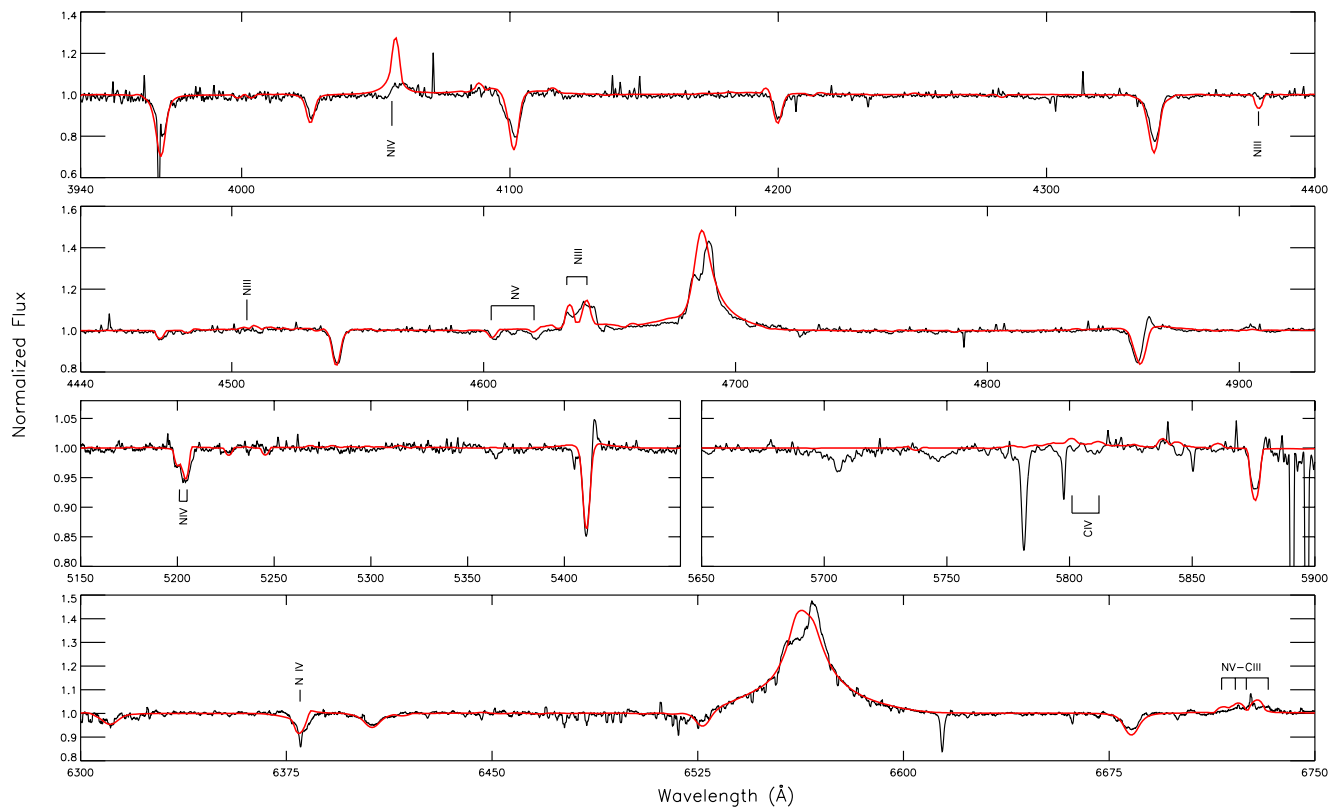


**Fig. A.6.** Best-fit model for HD 16691 (red line) compared to the *ELODIE* spectrum (black line)

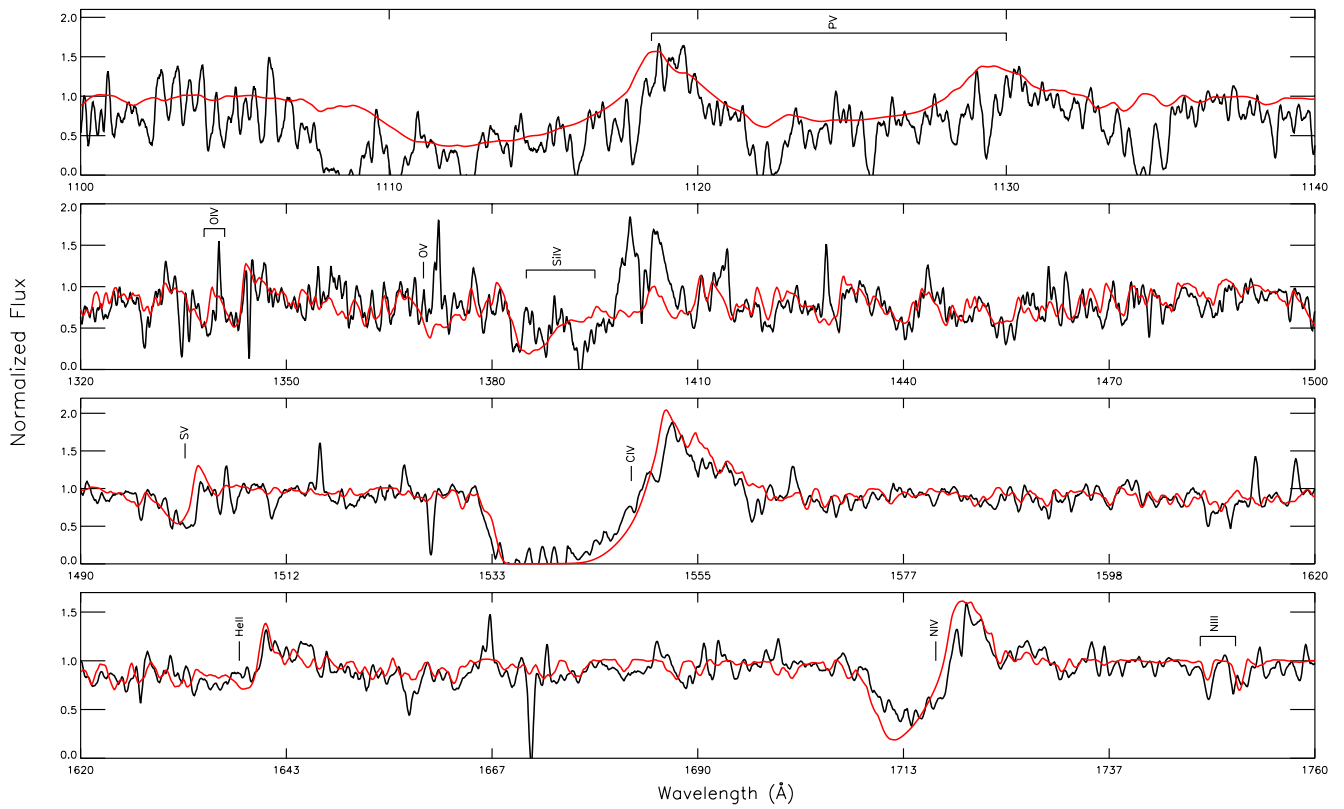


Fig. A.7. Best-fit model for HD 15570 (red line) compared to *FUSE* and *IUE* spectra (black line)

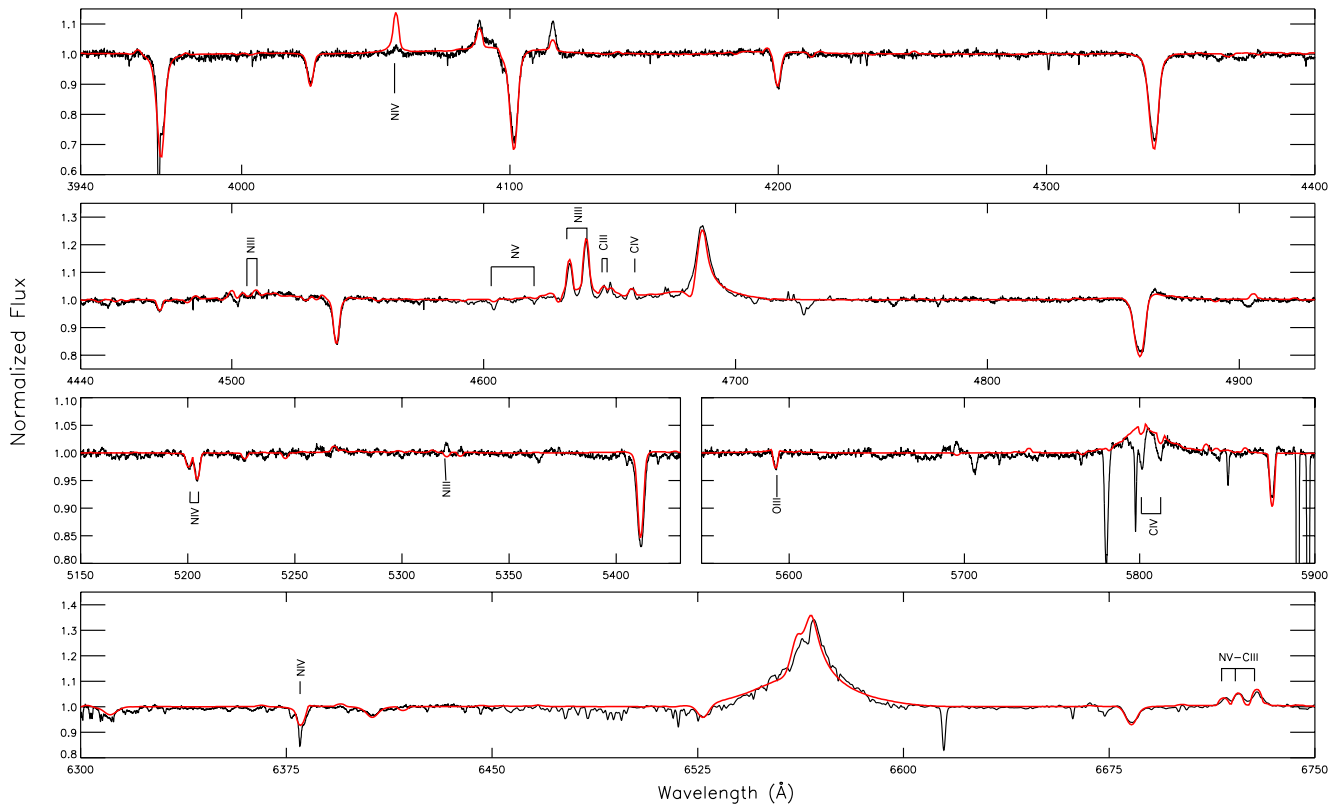


Fig. A.8. Best-fit model for HD 15570 (red line) compared to the *ELODIE* spectrum (black line)

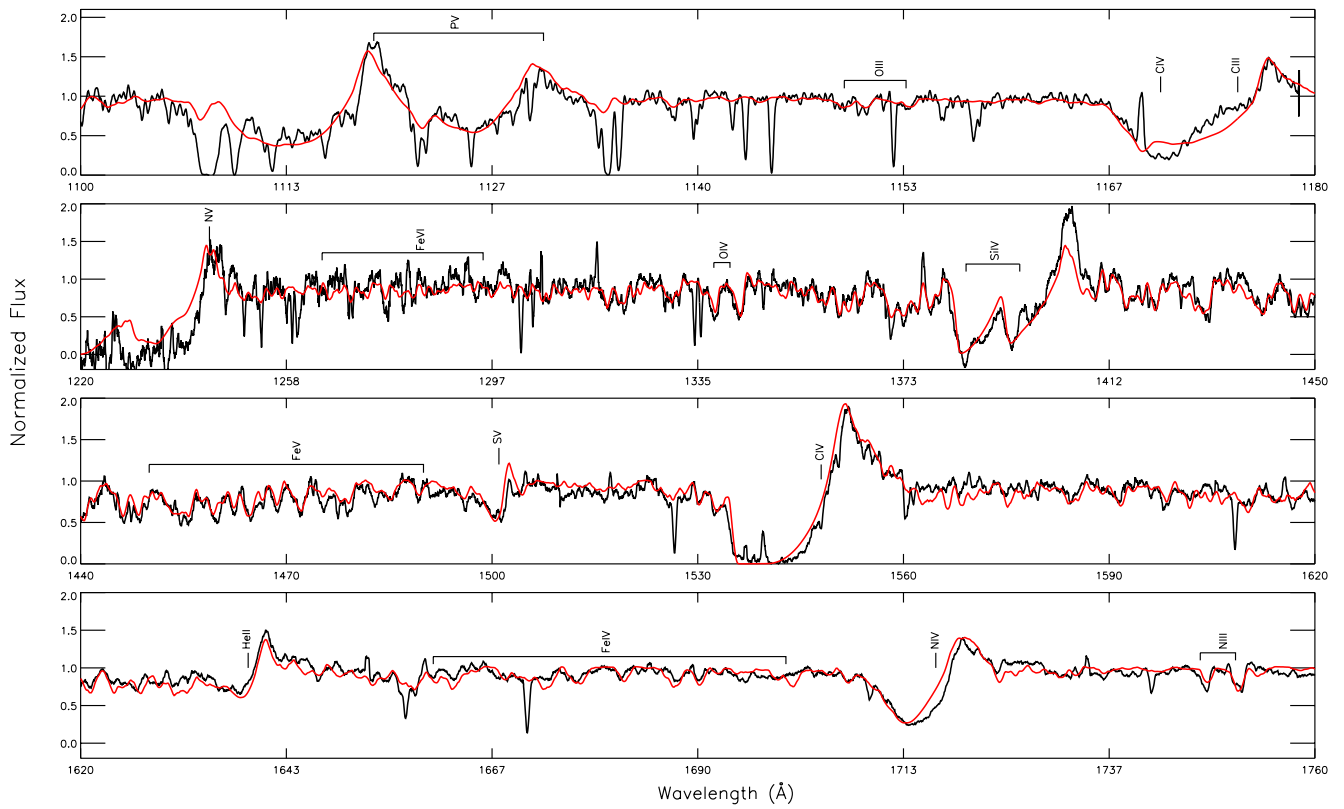


Fig. A.9. Best-fit model for HD 14947 (red line) compared to *FUSE* and *IUE* spectra (black line)

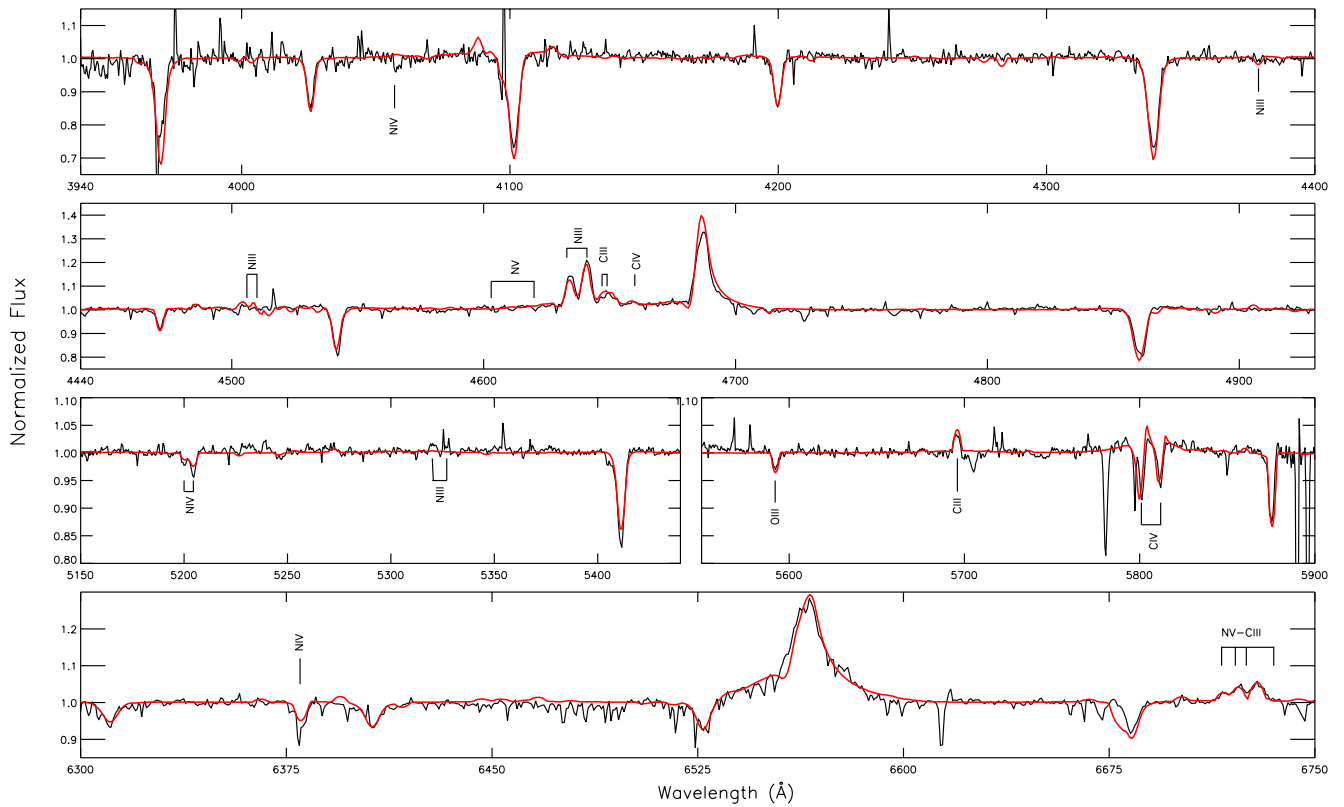


Fig. A.10. Best-fit model for HD 14947 (red line) compared to the *ELODIE* spectrum (black line)

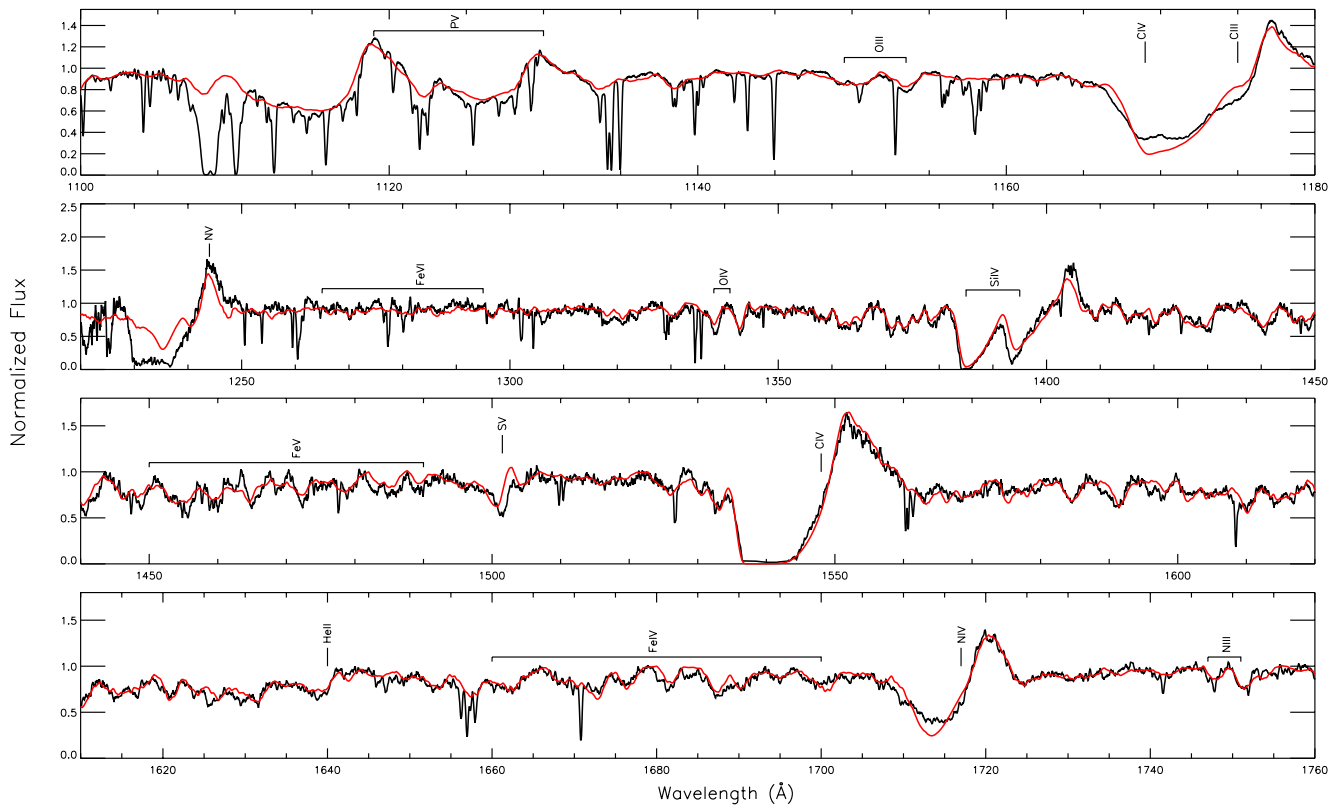


Fig. A.11. Best-fit model for HD 210839 (red line) compared to *FUSE* and *IUE* spectra (black line)

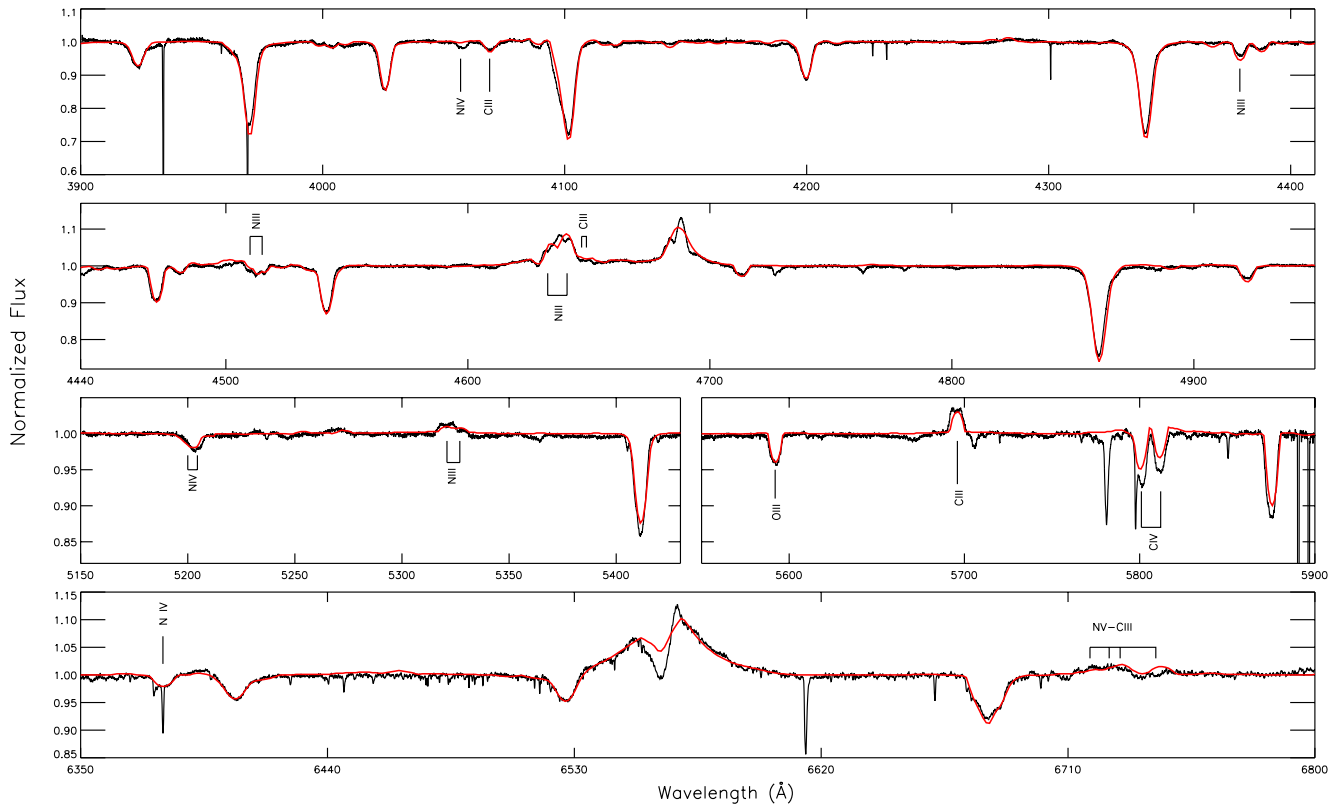
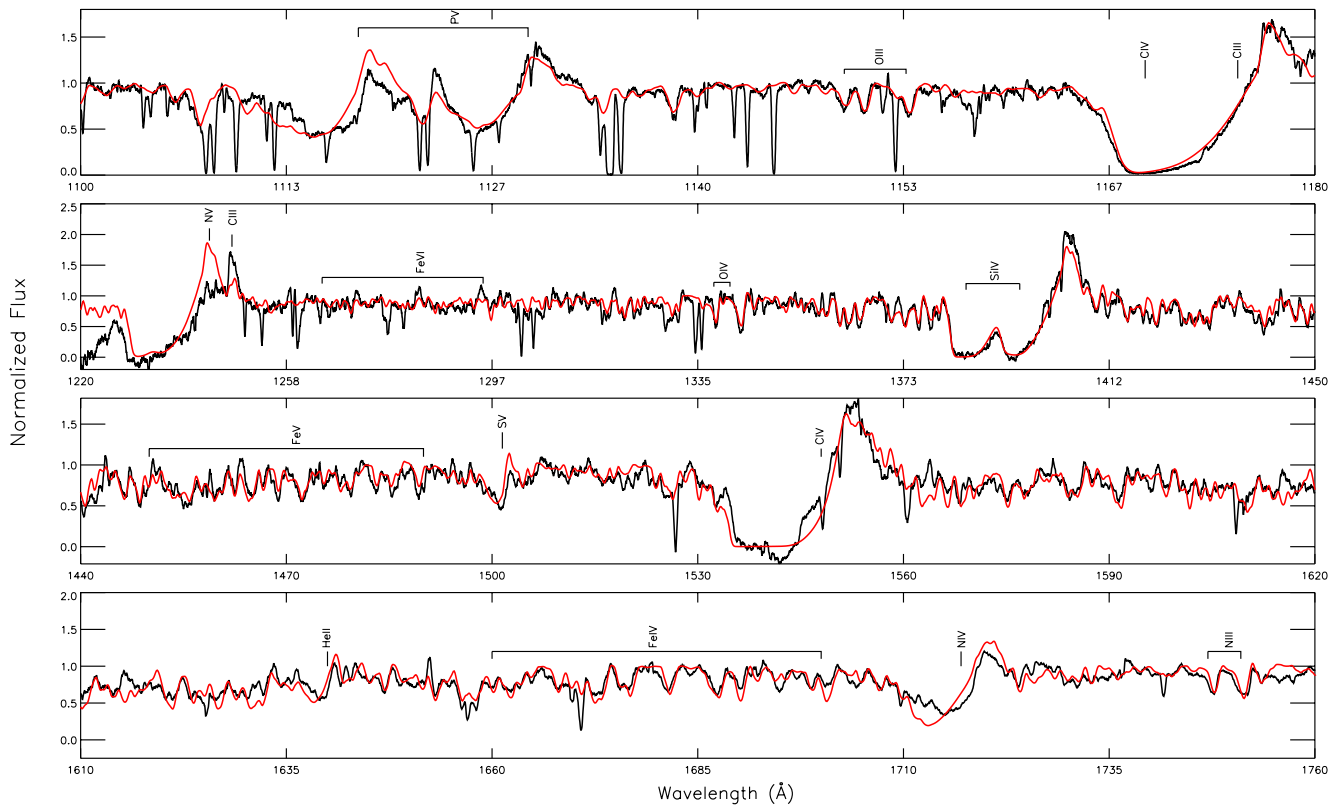
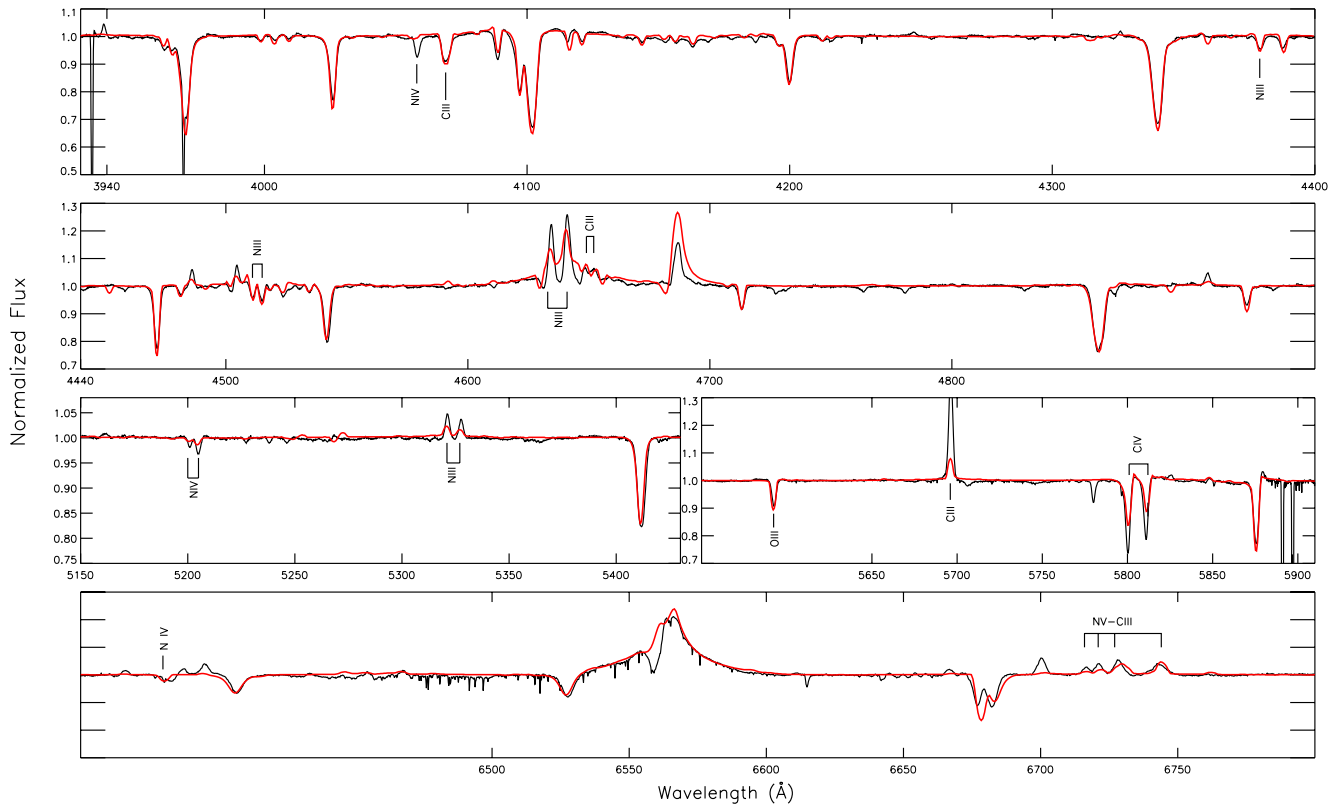


Fig. A.12. Best-fit model for HD 210839 (red line) compared to the *NARVAL* spectrum (black line)



**Fig. A.13.** Best-fit model for HD 163758 (red line) compared to *FUSE* and *IUE* spectra (black line)



**Fig. A.14.** Best-fit model for HD 163758 (red line) compared to the *UVES* spectrum (black line)



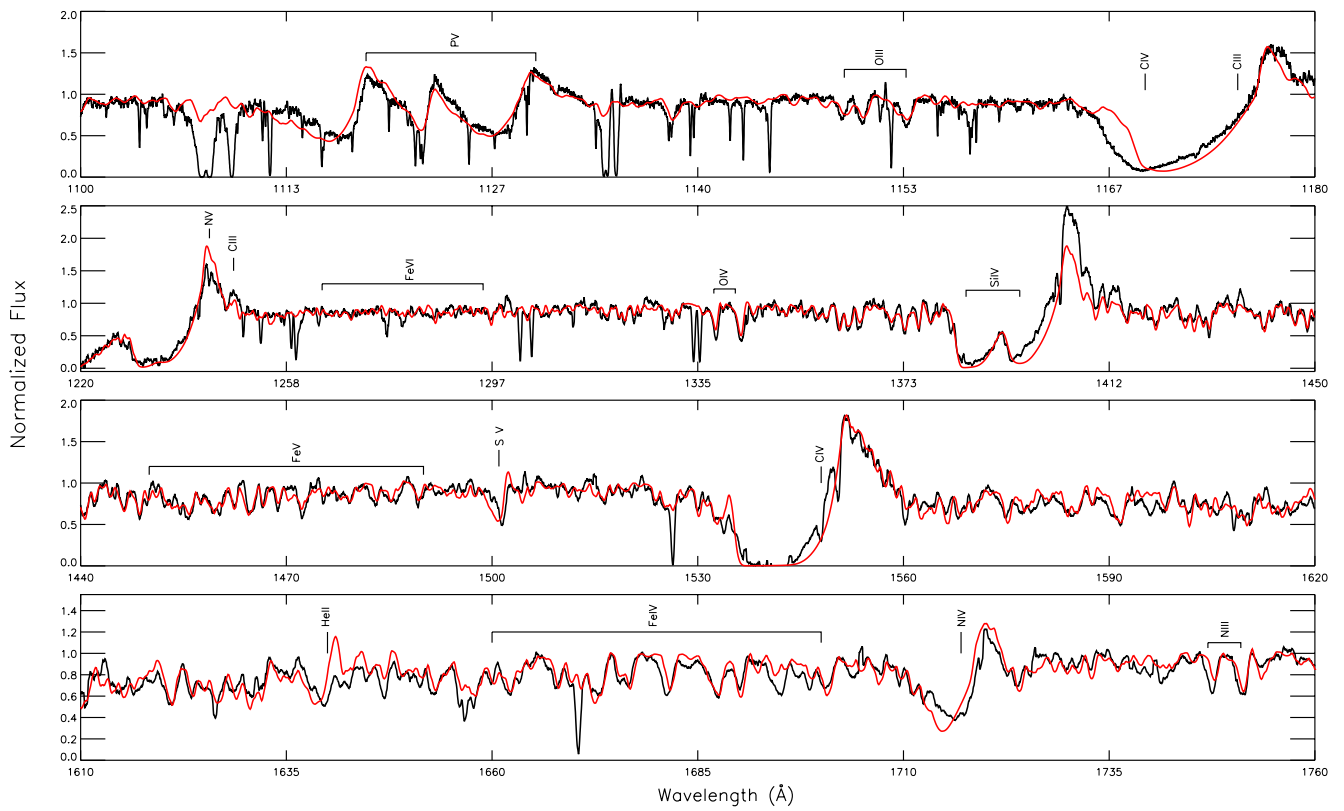


**Fig. A.15.** Best-fit model for HD 192639 (red line) compared to *FUSE* and *IUE* spectra (black line)

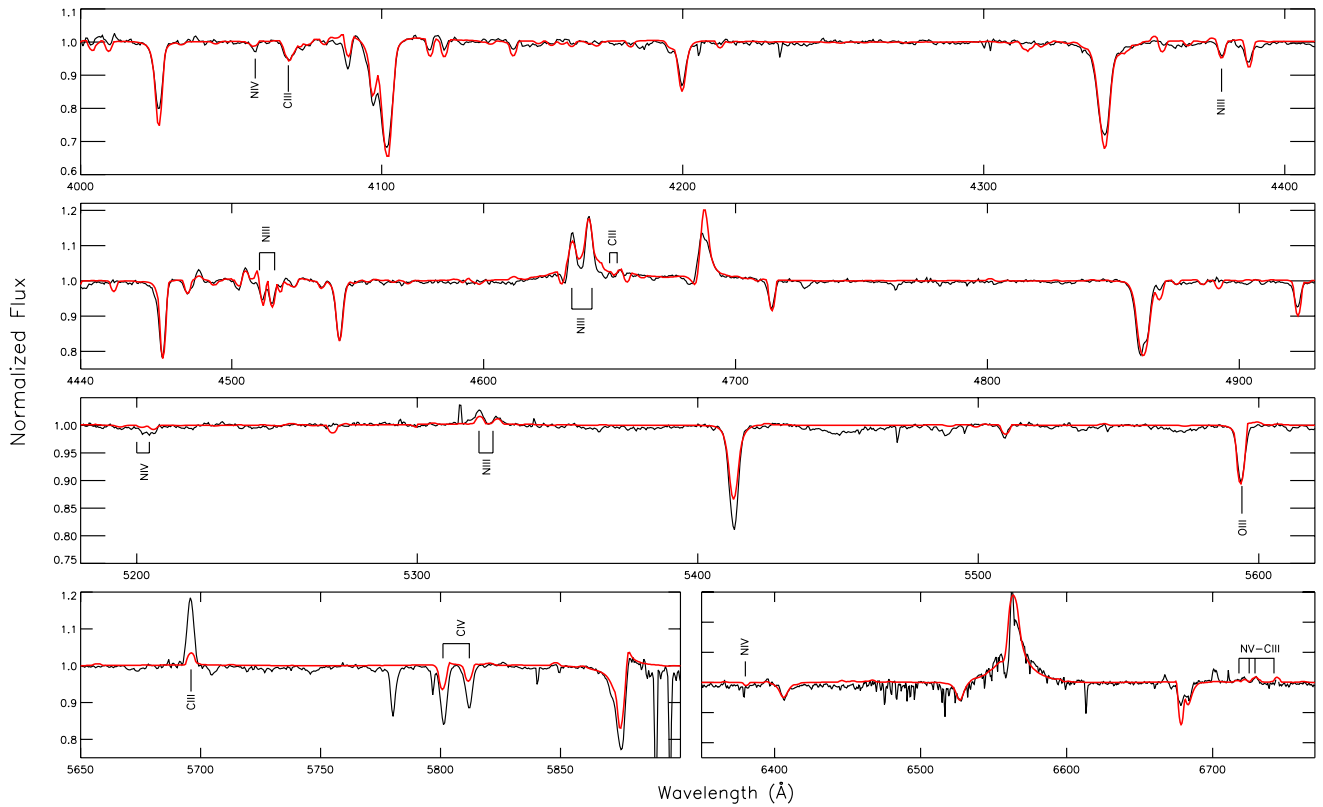


**Fig. A.16.** Best-fit model for HD 192639 (red line) compared to the *ELODIE* spectrum (black line)